Paper No.
03327

CORROSION 2003

The Effect of Cl^- and Acetic Acid on Localized CO_2 Corrosion in Wet Gas Flow

Yuhua Sun, Keith George, and Srdjan Nesic
NSF I/UCRC, Corrosion in Multiphase Systems Center
Institute for Corrosion and Multiphase Technology
Ohio University, Athens, OH 45701, U.S.A

ABSTRACT

Wet gas corrosion rates of C1018 and X65 steel have been measured at the top and bottom of a high pressure, 10 cm diameter horizontal pipeline under stratified flow conditions with different chloride (Cl^-) concentrations. Experiments were performed for 200 hours at 90°C, CO_2 partial pressure of 3.8 bar using a superficial gas velocity (Vsg) of 10 m/s and a superficial liquid velocity (Vsl) of 0.1 m/s. Three measurement techniques; ER, LPR, and WL were used simultaneously in the experiments. Localized corrosion occurred at the bottom of the pipe around the iron saturation point. The top of line was well protected by a thin corrosion product film and no localized corrosion was detected. C1018 and X65 have different sensitivities to pitting with a variation in Cl^- concentration. Thus the pitting density concept is proposed to describe localized corrosion behavior. Surface analysis on iron carbonate films, by SEM and XRD, revealed different film thicknesses and crystal structures from the top to the bottom of the pipe. Cross-sectional analysis indicates that the thin corrosion product film, usually less than 10 microns, attached to the metal surface, is responsible for the low corrosion rate on top of the line, while the thick and porous film formed on the bottom, generally detached from the metal surface, was responsible for the initiation of localized corrosion.

Before adding acetic acid (HAc) to the flow loop, a systematic glass cell test program was initiated using potentiodynamic sweeps to investigate the electrochemical properties of carbon dioxide corrosion in the presence of HAc. A standard rotating cylinder three-electrode setup was employed. Tests were performed to study the effect of HAc in solutions de-oxygenated using both nitrogen and carbon dioxide. The range of HAc concentrations was then expanded to study the effect of the concentration of HAc on the cathodic and anodic reactions in carbon dioxide solutions. The presence of HAc was found to not affect the corrosion rate of carbon steel at low temperature since the main cathodic reaction (hydrogen ion reduction) was found to be under charge transfer control. The limiting current was strongly affected by the HAc concentrations, but the charge transfer mechanism was not changed. The anodic reaction was retarded with increasing HAc concentrations but the mechanism stayed the same. The effect of pH, temperature and rotational velocity was also studied.

Key words: C1018 steel, X-65 steel, wet gas, localized corrosion, stratified flow, cross section, surface analysis, pitting density, super-saturation, acetic acid, potentiodynamic sweeps

INTRODUCTION

Natural gas does not emerge from the reservoir "pure" and is always accompanied by various amounts of water, carbon dioxide, hydrogen sulfide, and organic acids. These substances combine to give rise to a very aggressive environment where the survival of mild steel is not guaranteed. The multi-phase mixture of gaseous and liquid hydrocarbons, water, CO_2 and H_2S moves through the gas pipelines in a variety of complicated multi-phase flow patterns such as annular, slug and stratified flow, depending on the terrain topography and the individual phase flow rates. It is well known that flow can accelerate corrosion of mild steel by increasing the mass transfer rates of corrosive species and/or by damaging the protective films formed on the steel surface[1].

In wet gas corrosion research, there are only a handful of studies that relate to field experience, some focusing on corrosion management[2] and control[3], others reporting actual case histories[4]. In most studies the focus was on top-of-line corrosion[4-6] where high uniform corrosion and sometimes localized attack were associated with rapid condensation of water by external cooling. There are no studies reported in the open literature, which investigate the nature and magnitude of the attack in wet gas transport in the presence of low condensation rates, typical for well-insulated pipelines.

Localized corrosion is not well understood even though some research has been done in this field. For example Xia et al.[7] studied pitting corrosion of carbon steel at room temperature and atmospheric pressure and suggested that galvanic couples were responsible for initiation and development of pits. Schmitt et al.[8-10] performed numerous experiments and concluded that the onset of localized attack was related to high near-wall levels of turbulence and the intrinsic growth stresses in the corrosion product scale. Nyborg[11] investigated initiation and growth of mesa attack and proposed a mechanism involving film breakdown. Actually, the common underlying theme in all these studies is that localized attack in CO_2 corrosion of mild steel is always associated with the formation and breakdown of protective iron carbonate films. However, it needs to be stressed that all these studies have been conducted in single-phase water flow. There are no studies on localized corrosion conducted under wet gas flow conditions. Hence, an extrapolation of these results achieved in single-phase flow to multiphase flows under field conditions is uncertain.

Previous experiments in multiphase flow from this laboratory have been conducted at both high and low temperature. The low temperature (40°C) tests[12] concluded that localized corrosion does not occur in the absence of corrosion product film. The high temperature (90°C) tests covered the hydrodynamic effects of gas-water-oil flow[13], where even the presence of small amounts of oil was found to reduce the corrosion rate and prevent localized corrosion. Other parameters, such as the pH, pressure, and hydrodynamic effects, were also tested based on the recent parametric study from a mechanistic corrosion model [14]. The present work focuses on the Cl^- effect on localized CO_2 corrosion in stratified flow under natural condensation wet gas transportation conditions.

Some understanding of the role of HAc in CO_2 corrosion comes from the field experience, as related to the so-called Top-of-Line-Corrorion[4]. But, very few systematic studies have been performed in the laboratory. Little or no information exists about the fundamental effect of HAc on the anodic and cathodic reactions. Hedges and McVeigh[15] reported a mild increase in the cathodic reaction in the presence of HAc although their results were not fully conclusive. The work of Crolet et al.[16] suggests that the presence of HAc inhibits the anodic (iron dissolution) reaction. Garsany et al.[17] published work-using voltammetry to study the effect of acetate ions on the rates and mechanisms of corrosion using a rotating disc electrode (RDE) on film-free surfaces. The voltammograms show two waves, which they

attributed to hydrogen and acetic acid reduction on the steel surface. They argue that since acetic acid dissociation can occur very quickly it is not possible to distinguish the reduction of hydrogen ions from acetic acid at the electrode surface.

EXPERIMENTAL

Flow Loop and Test Section

A unique, 18 m long, 10 cm diameter, high pressure, high temperature inclinable multiphase flow loop was used to study wet gas CO_2 corrosion. The entire loop is manufactured from 316L stainless steel. The test section has three pairs of ports at the top and the bottom, which are used to insert flush-mounted electrical resistance (ER), linear polarization resistance (LPR), and weight loss (WL) probes for corrosion rate measurements. A detailed description of the flow loop and test section can be obtained elsewhere[13].

Glass Cells

A schematic of the test cell is shown in Figure 1. A three-electrode system was used with the counter electrode made of platinum and the reference connected to the cell by a Luggin capillary tube. A preconditioning cell was used to ensure a constant HAc concentration in the test cell. Since HAc is volatile, the preconditioning cell ensures that any gaseous HAc is in equilibrium with the flowing carbon dioxide and a constant concentration of HAc will be maintained in the test cell. The use of a gas bubbler downstream of the test cell ensures a positive pressure of carbon dioxide in the test cell.

Specimen Preparation

In the present study, two carbon steels (C1018 and X-65) are used for WL and cross-sectional analysis. The coupons are circular with a diameter of 11.6 mm and a thickness of 3.1 mm. The chemical compositions of the two steels are given in Tables 1 and 2. The specimens used in the glass cells were 5.4 cm^2 in area and the chemical composition is given in Table 3.

Prior to testing, the specimen were polished by silicon carbide paper up to 600 grit, then rinsed with isopropyl alcohol, and air dried. The specimen for weight loss analysis were weighed and numbered and then introduced into the system immediately.

The post-test cleaning procedure was performed by immediately rinsing the specimen with isopropyl alcohol, air drying, and then storaged for surface analysis at a later date. For WL analysis, the specimen were pickled in an inhibited 10% hydrochloric acid for removal of corrosion products, then neutralized in alkali, rinsed with distilled water and alcohol, air dried and weighed for mass loss measurements. After this, the specimen is examined under a Metallurgical Microscope (MM) for the localized attack measurements.

For surface analysis specimens, after the surface of the specimen is examined by Scanning Electron Microscopy/Energy Dispersive Spectrum (SEM/EDS) and X-ray Diffraction (XRD), the specimens were prepared for the final step—cross-sectional analysis, to examine the thickness and morphology of the corrosion product film. This is achieved by first embedding the coupon into epoxy, followed by cutting across the specimen surface. A MM and/or SEM was used to generate photographs of the cross section.

Operational Procedure for Flow Loop

The experimental system is filled with a predetermined amount of a NaCl solution. The system is then deoxygenated by flushing carbon dioxide through the system until the level of dissolved oxygen is below 10 ppb. The system is then heated to the test temperature and pressurized to the test pressure. The flow rates of the gas and liquid were then set. Once the flow was stabilized, corrosion monitoring probes were then inserted into the flow loop.

The test matrix for this work is shown in Table 4. The superficial liquid velocity (Vsl) of 0.1 m/s was used at superficial gas velocities (Vsg) of 10 m/s at a pressure of 4.45 bar and a temperature of 90°C. At this condition, the flow regime is in stratified flow according to the pressure drop measurement results shown in Figure 2. The ER probe is made from C1010, and LPR probe is made from C1018.

Operational Procedure for Glass Cells

To begin an experiment, the experimental apparatus was assembled, a salt solution was prepared and added to the cell, and then de-oxygenation occurred for one hour using carbon dioxide gas. The appropriate amount of HAc was then added to the cells and de-oxygenation occurred for an additional 30 minutes. The pH was monitored before and after the HAc addition to ensure the fluid composition was similar between test runs. The electrode was then immersed into the test solution and all electrical connections were made. The electrode's rotational velocity was set and allowed to rotate for approximately 30 additional minutes before any electrochemical measurements were carried out.

The test matrix for the work is shown in Table 5. The potentiodynamic sweeps were conducted at a sweep rate of 0.2 mV/s and the solution resistance was measured using electrochemical impedance spectroscopy (EIS) and corrected for. The potentiodynamic sweeps were conducted at constant pH with the pH adjustment occurring after each sweep. During the anodic sweep for example, the system pH was set to 4.00 ± 0.01 and the sweep started. Due to iron dissolution, the pH of the system may rise to 4.08 by the end of the sweep. The pH was then adjusted using HCl before the beginning of the next sweep. Anodic sweeps were limited to polarization less than 200 mV above the corrosion potential to limit excessive iron concentrations in the test cell. The LPR measurements were taken at ±5 mV around the corrosion potential.

RESULTS ON THE EFFECT OF Cl^-

Test with no NaCl in the Flow Loop

In the test without Cl^-, the pH and dissolved iron content increased with time as shown in Figure 2. The trend for both ferrous iron concentration and pH suggests that the rise of the pH was due to the corrosion (iron dissolution) process. The solution was under-saturated at the beginning of the test, but reached super saturation (SS) at the end, as indicated by Figure 3.

Figure 4 shows the time evolution of uniform corrosion rate from ER and LPR measurements. In this particular test, the two techniques gave totally different results. For example, at the bottom of the pipe, the corrosion rate measured by ER remained high for the whole duration of the experiment, while the LPR showed a relatively high corrosion rate at the beginning, but a stabilized low corrosion rate at the end of the test, indicating the formation of a protective film. Two techniques showed the corrosion rate difference in two orders of magnitude.

The third technique, WL method was also used in the test. The integrated corrosion rates over the entire period of time are shown in Figure 5 for different methods. It is seen that WL method indicated high corrosion rates at the bottom for both materials, C1018 and X-65. The results from WL are in good agreement with that from ER. Thus the LPR results are considered to be at fault in this case.

The specimen was visual examined first after the test and no localized attack was observed. However, microscopy inspections revealed that a highly spread non-uniform attack did occur on both materials, as shown in Figure 6. In fact, the hills and valleys, and sometimes mesa attack occupied the whole specimen surface. It is estimated that 50% of the surface area was covered by the grooves. The height distance between the "hills" and "valleys" is described as the magnitude of the localized corrosion rate in this paper, and the value is added in Figure 5 to the uniform corrosion rate.

Test with 0.1% NaCl

Similar to the test without NaCl, the pH and dissolved iron content increased during the test, as shown in Figure 7. The solution again started out as under-saturated and ended up being super saturated. Figure 8 shows the change of uniform corrosion rate with time measured by ER and LPR methods. At the beginning of the test, both ER and LPR bottom gave the same corrosion rate results. But after an initial period of time, LPR bottom showed a greatly decreased corrosion rate again and finally stabilized at a much lower value compared to the ER method, as reflected in the test without Cl^-. The corrosion rate on the top, measured by the ER method, shows high corrosion at the beginning and then decreased to a relative stable and small value in a short time. Although the solution resistance was greatly decreased by adding NaCl, the top LPR measurements were still not stable. This probably suggests that the water on the top was predominantly from condensation. The corrosion rates have orders of magnitude difference between the bottom and top, reflected by all the three measurement techniques, as shown in Figure 9. Weight loss results are more comparable to ER results, while LPR deviates from the other two methods. However, there is a major difference in this test compared to the previous test with no NaCl. Some localized attack in the form of pitting or mesa corrosion was found on the bottom of the C1018 steel coupons (see Figure 10). X-65 was still attacked by non uniform corrosion and has the similar very rough surface as observed in the test without NaCl. The top specimen of both materials was well protected by thin films and no localized corrosion was found. This can be seen by cross-section analysis shown in Figure 10.

Test with 1% NaCl.

The results obtained in this test are shown in Figure 11, Figure 12, and Figure 13. This test was stopped after 100 hours due to the gas pump failure. But the experiment was long enough to show the trend and allow comparison with the previous two tests. For example, the pH and Fe^{2+} concentration change obey the same trend as before (Figure 11), LPR bottom measurement again shows the protective film formation after an initial time (Figure 12). All the other corrosion rates measurements show the similar trend to the other two tests, but have slightly higher values (Figure 13). Localized corrosion occurred on both materials with a small percentage of surface area attacked, which is different from the last two tests. Cross-sectional analysis (Figure 14) again shows protective film on the top specimen and a very porous film on the bottom specimen.

DISCUSSION ON THE EFFECT OF Cl^-

Figure 15 shows the effect of NaCl concentration on the bottom corrosion rate from WL method for both materials. It is seen that Cl^- has some effect on both uniform and localized corrosion rate on the bottom of the line. In all cases, localized corrosion occurred on both materials. However, this Figure cannot tell more about the nature of the localized attack. As described above, some of the localized attack was widespread on the specimen surface, with hills, valleys, and mesa typed corrosion covering the whole surface, while on others it was a true local phenomenon. Based on this consideration, pitting density is probably a more accurate concept to describe the localized corrosion. It is defined as the ratio of pitted area or the area suffering localized attack to the total area of specimen. The results are shown Figures 16 and 17. With an increase in Cl^- concentration, the pitting density decreased, which means that the localized attack tends to be more "local". C1018 and X65 seem to have different sensitivity with respect to Cl^- concentration.

In all the three experiments, the water chemistry was changing, from an under-saturated iron solution at the beginning to a very super-saturated iron solution at the end of each test. This might create a favorable environment for initiation of localized corrosion. Figure 17 may explain what happened. It seems that the super saturation point played a very important role in the onset to localized corrosion. Localized corrosion does not occur in either under-saturated solution or highly super-saturated solution. The tests presented in this work happened to fall in a range around the saturation line, and the localized corrosion was then triggered. Given the same environment parameters, the Cl^- affects the solution super saturation level through ionic strength and solubility.

Without exception, no localized corrosion was found on top of the line in any of the tests. The corrosion rate was orders of magnitude lower than the bottom, as shown in Figure 18 by ER measurement. Since the flow regime is in stratified flow, the water chemistry on the top of the line is different from the bottom. Under the flow conditions tested, the water on the top of the pipe could be from two sources: either from the droplets entrained in the gas phase, which should have the same chemistry as the water at the bottom; or from the pure condensing water, whose chemistry is very different. However, according to the cross-section images, the amount of water on the top must have been very small, enabling formation of a very thin film, which was rapidly saturated by $FeCO_3$ and lead to a protective layer. This layer was not affected by the presence of Cl^-. Admittedly the concentration of Cl^- at the top was most likely lower due to the presence of condensed water. Thus no localized corrosion was found on the top and the uniform corrosion rate remained low.

Throughout the three experiments, ER and WL measurements were in good agreement, while LPR measurements deviated. The reason for this behavior could be the polarization, which disturbs the corrosion process. This would become more important when solution is around saturation point. Cathodic polarization consumes hydrogen ions and creates locally a higher pH, while the anodic scan releases more ferrous ion and increase the iron concentration on the steel surface. A higher pH and iron concentration could cause the high super saturation locally, which speeds up the film formation process.

The surface analysis for the corroded specimen provides solid backing of the corrosion rate measurements. XRD results show that the corrosion product is mainly $FeCO_3$ (Figure 19). This is valid for both top and bottom specimen in all the three tests. The carbonate layer on the top seems more protective with smaller crystals, indicating higher super saturation and faster precipitation, than those formed on the bottom with more porous, less crystalline structure, as seen from Figure 20. The cross-sections of the specimen (Figure 6, Figure 10, and Figure 14) show the thin, protective film on the top

and the thick, non-protective film on the bottom. The thickness of the top film is generally less than 10 μm, while the film formed on the bottom is more than 100 μm. In addition, at the bottom, the film is detached from the metal surface over large areas, which provided very poor resistance to corrosion.

RESULTS AND DISCUSSION ON THE EFFECT OF HAc

Initially, potentiodynamic sweeps were performed in 3% sodium chloride solution flushed with nitrogen for a concentration range of 0 to 1000 ppm HAc at pH 4. The pH was held constant to distinguish the effect of the acetic species on the cathodic and anodic reactions from the effect of H^+ (pH). At a constant pH, the concentration of hydrogen ions is fixed, and the effect of the acetic species on the cathodic and anodic reactions could be seen. The results are shown in Figure 21. There is a clear acceleration of the cathodic limiting current density with increased concentrations of HAc. The anodic reaction was inhibited with an increase in the HAc concentration, which has also been reported by Crolet[16]. Since the cathodic charge transfer reaction did not move significantly with increasing concentrations of HAc, reduction of hydrogen ions is more likely occurring rather than direct reduction of HAc.

The corrosion rates measured by LPR and Tafel analysis are shown in Figure 22. It should be stressed that the corrosion rates measured using LPR were taken within approximately 30-45 minutes of exposure to the test solution. The corrosion rates were estimated using a cathodic Tafel slope of 120 mV/dec and an anodic Tafel slope of 80 mV/dec. The corrosion rates estimated using these two methods are similar since the cathodic and anodic reactions are most likely under charge-transfer control for the hydrogen ion reaction. This is supported by the fact that the limiting current increased almost nine times (see Figure 21) while the corrosion current did not increase much. This indicates that acetic acid acts primarily as a source of hydrogen ions and does not affect the charge transfer reactions. This also has been reported by Garsany et al.[17]

The effect of adding carbon dioxide was studied at the same concentrations of HAc. The results for the 0 ppm HAc concentrations are shown in Figure 23. It is evident from Figure 24 that the limiting current density of the cathodic reaction is increased slightly in the presence of carbon dioxide. The anodic reaction in nitrogen solutions was unaffected by an addition of carbon dioxide at all concentrations of HAc. The 100 and 1000 ppm HAc potentiodynamic sweeps are shown in Figure 24 and 25, respectively. At 100 ppm of HAc, the limiting current densities of the cathodic reactions for both solutions are significantly increased when compared to the 0 ppm HAc limiting current densities. Again a slight increase in the limiting current density of the cathodic reaction in the presence of carbon dioxide was found. A similar trend is found upon a further increase in the HAc concentration to 1000 ppm.

The effect of HAc concentration was studied in 3% sodium chloride solutions adjusted to a pH of 4. The HAc concentration was varied from 0 to 5000-ppm and the cathodic and anodic sweeps are shown in Figures 26 and 27, respectively. As argued above, with increasing concentrations of HAc, the limiting current density of the cathodic reaction was accelerated. However, with increasing concentrations of HAc the anodic reaction was retarded. While not shown, the retardation in the anodic reaction was also evident in solutions containing nitrogen.

The effect of HAc concentration on the CO_2 corrosion rate is shown in Figure 28. As before, the LPR measurements were taken within 30-45 minutes of electrode exposure to the test solution. As in cases where no CO_2 was present, the corrosion rates are approximately the same, regardless of HAc concentration, since the HAc is acting only as an extra source of hydrogen and the reactions are under

charge-transfer control so availability of hydrogen ions is not rate limiting. Selected potentiodynamic sweeps containing varying concentrations of HAc, which have already been shown in Figures 26 and 27, have been shown again in Figures 29 and 30, with the fitted Tafel slopes used in the LPR calculation.

The effect of pH on the potentiodynamic sweeps was studied in 3% sodium chloride solutions containing 100 ppm HAc, adjusted in the pH range of 4 to 6. The results are shown in Figure 31. As the pH was increased from 4 to 5, the anodic reaction rate increased. But a further increase in pH from 5 to 6 does not result in a further increase in the anodic reaction rate. This has been seen in solutions with carbon dioxide in the past. According to Bokris[18], the hydroxyl molecule (OH^-) acts as a catalyst in the dissolution step for iron. At higher pH, the surface of the steel is saturated with the hydroxyl molecules and the rate-limiting step is the iron leaving the metal lattice. This saturation with hydroxyl molecules in carbon dioxide solutions occurs between a pH of four and five. The cathodic reaction however, is retarded by an increase in pH due to less hydrogen ions being available for reduction.

The effect of velocity (500-4000 rpm) was studied using potentiodynamic sweeps performed in 3% sodium chloride solutions containing 100 ppm HAc and at pH 4. The results are shown in Figure 32. According to theory, the limiting currents should increase by a factor of 1.6 with each doubling of velocity since the Reynolds number term, in the Sherwood number correlation, is raised to the 0.7 power. The increase in the limiting current was measured to be approximately 1.8-2 when the velocity was doubled. The corrosion potential, as well as the anodic reaction, does not change with velocity suggesting a constant corrosion rate. This appears to support the assumption that the corrosion rate under the conditions studied was charge transfer controlled.

The effect of temperature on the potentiodynamic sweeps was studied in 3% sodium chloride solutions containing 100 ppm HAc. The results are shown in Figure 33. There is a clear acceleration of both the cathodic and anodic reaction rates with an increase in temperature. Also, with an increase in temperature, the corrosion potential is shifted to more negative values due to the anodic reaction rate increasing more than the cathodic one. The corrosion rates measured by LPR and calculated from Tafel slopes are shown in Figure 34 and the two methods are in good agreement.

CONCLUSIONS

- Under the multiphase test conditions, localized corrosion occurred at the bottom of line on both C1018 and X65 materials but with different pitting densities. Pitting density is thus recommended to use when describing the localized corrosion behavior.
- Neither C1018 nor X-65 suffered localized attack at the top of line under stratified flow conditions.
- Cl^- content is important in the onset of localized corrosion since it largely affects the ionic strength and thus super-saturation level of the solution.
- C1018 and X-65 steels showed somewhat different sensitivity to pitting density with respect to Cl^- concentration.
- It has been shown that the corrosion rate of carbon steel in the presence of HAc is not significantly affected by the HAc at room temperature since the corrosion rate is dominated by charge transfer of the H^+ reduction reaction.
- HAc did not affect the charge transfer mechanism of the cathodic reaction but the limiting current density was strongly affected.

- The anodic reaction was retarded with increasing HAc concentrations, but the mechanism remained the same.

ACKNOWLEDGEMENTS

The authors wish to thank the Institute for Corrosion and Multiphase Technology at Ohio University and its member companies for the financial support of this research.

REFERENCES

1. S. Nesic, M. Nordsveen, R. Nyborg, and A. Stangeland, "A Mechanistic Model for CO_2 Corrosion with Protective Iron Carbonate Films," Corrosion/2001, paper no. 01040, (Houston, TX: NACE International, 2001).
2. S.D. Kapusta, B.F.M. Pots, and R.A. Connell, "Corrosion Management of Wet Gas Pipelines," Corrosion/99, paper no.45, (Houston, TX: NACE International, 1999).
3. Y.M. Gunaltun and A. Belghazi, "Control of Top of Line Corrosion by Chemical Treatment," Corrosion/2001, paper no.33, (Houston, TX: NACE International, 2001).
4. Y.M. Gunaltun, D. Supriyatman, and J. Achmad, "Top of Line Corrosion in Multiphase Gas Lines, A Case History," Corrosion/99, paper no.36, (Houston, TX: NACE International, 1999).
5. B.F.M. Pots and E.L.J.A Hendriksen, "CO_2 Corrosion under Scaling Conditions- the Special Case of Top-Of-Line Corrosion in Wet Gas Pipelines," Corrosion/2000, paper no.31, (Houston, TX: NACE International, 2000).
6. Y.M. Gunaltun and T. Chevrot, "Requirements for Inhibition of Localized Corrosion," Corrosion/99, paper no.6, (Houston, TX: NACE International, 1999).
7. Z. Xia, K.C. Chou, and Z. Szklarska-Smialowska, "Pitting Corrosion of Carbon Steel in CO2-Containing NaCl Brine," Corrosion, 45(8), p.636,1989.
8. G. Schmitt, T.Gudde, and E. Strobel-Effertz, "Fracture Mechanical Properties of CO2 Corrosion Product Scales and Their Relation to Localized Corrosion," Corrosion/96, paper no.9, ((Houston, TX: NACE International, 1996).
9. G. Schmitt and M. Mueller, "Critical Wall Shear Stresses in CO2 Corrosion of Carbon Steel," Corrosion/99, paper no.44, ((Houston, TX: NACE International, 1999).
10. G. Schmitt and S. Feinen, "Effect of Anions and Cations on The Pit Initiation in CO2 Corrosion of Iron and Steel," Corrosion/2000, paper no.1, (Houston, TX: NACE International, 2000).
11. R. Nyborg, "Initiation and Growth of Mesa Corrosion Attack During CO2 Corrosion of Carbon Steel," Corrosion/98, paper no.48, (Houston, TX: NACE International, 1998).
12. Y-H Sun, T. Hong, and W. P. Jepson, "Corrosion under Wet Gas Conditions," Corrosion/01, paper no.01034, (Houston, TX: NACE International, 2001).
13. Y-H Sun, T. Hong, and C. Bosch, "CO2 Corrosion in Wet Gas Pipelines at Elevated Temperature," Corrosion/02, paper no.02281, (Houston, TX: NACE International, 2002).
14. S. Nesic, K-L. J. Lee, and V. Ruzic, "A Mechanistic Model of Iron Carbonate Film Growth And The Effect on CO2 Corrosion of Mild Steel," Corrosion/2002, paper no.02237, (Houston, TX: NACE International, 2002).
15. Hedges, B, and McVeigh, L., "The Role of Acetate in CO_2 Corrosion: The Double Whammy," CORROSION/1999, Paper No. 21, (Houston, TX: NACE International, 1999).
16. Crolet, J-L., Thevenot, N., and Dugstad, A., "Role of Free Acetic Acid on the CO_2 Corrosion of Steels," CORROSION/1999, Paper No. 24, (Houston, TX: NACE International, 1999).
17. Garsany, Y., Pletcher, D., Hedges, B., "The Role of Acetate in CO_2 Corrosion of Carbon Steel: Has the Chemistry Been Forgotten?" CORROSION/2002, Paper No. 2273, (Denver, CO: NACE International, 2002).

18. Bokris, J. O'M, Reddy, A.K.N, Modern Electrochemistry, New-York, Plenum Press, 1973.

Table 1. Chemical Composition of Type C1018 Carbon Steel (wt.%)

C	Si	P	S	Mn	Al	Fe
0.21	0.38	0.09	0.05	0.05	0.01	balance

Table 2. Chemical Composition of 5LX65 Steel (wt.%)

C	Si	P	S	Mn	Nb	V
0.07	0.24	0.014	0.011	1.26	0.033	0.04

Table 3. Chemical Composition of 5LX65 Used in RCE (wt%)

Cr	Mo	S	V	Si	C	Fe	Ni	Mn	P
0.011	0.103	0.004	0.055	0.240	0.150	Balance	0.020	1.340	0.011

Table 4. Test Matrix for the Flow Loop Experiments

Liquid phase	0, 0.1%, 1% NaCl
Total pressure	4.45 bar
CO_2 partial pressure	3.75 bar
Temperature	90°C
Superficial gas velocity	10 m/s
Superficial liquid velocity	0.1 m/s
Material	C1018, X65, and C1010
Measurement techniques	ER, LPR, and WL

Table 5. Test Matrix for the Glass Cell Experiments

Liquid Phase	3 % NaCl
Gases used for De-oxygenation	N_2 and CO_2
HAc Concentration	0 – 5000 ppm
Temperature	22°C
pH	4.00
Rotational Velocity	1000 rpm
Material	X65
Measurement Techniques	LPR, EIS, Potentiodynamic Sweeps

Table 6. Super-Saturation Table and Estimated Pitting Density

NaCl, %	At the beginning of test			At the end of test			Pitting density = pitted area/total area	
	Measured pH	Measured Fe^{2+}	Super saturation level	Measured pH	Measured Fe^{2}	Super saturation level	C1018	X-65
0.0	4.65	20	0.60	4.94	50	5.5	50%	50%
0.1	4.65	20	0.42	5.13	100	30.9	9%	50%
1.0	4.65	20	0.27	5.3	100	21.4	3%	5%

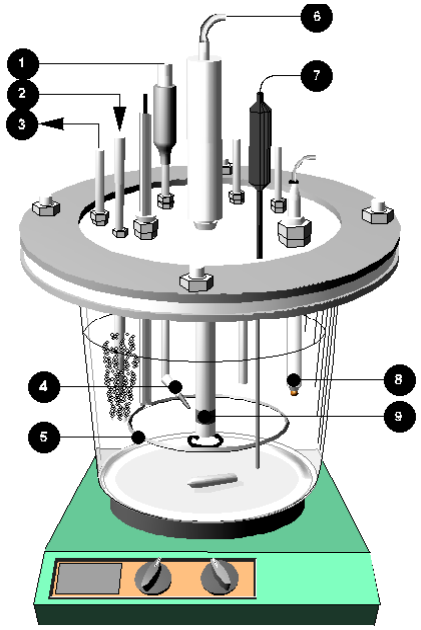

Figure 1. Diagram of the Test Cell

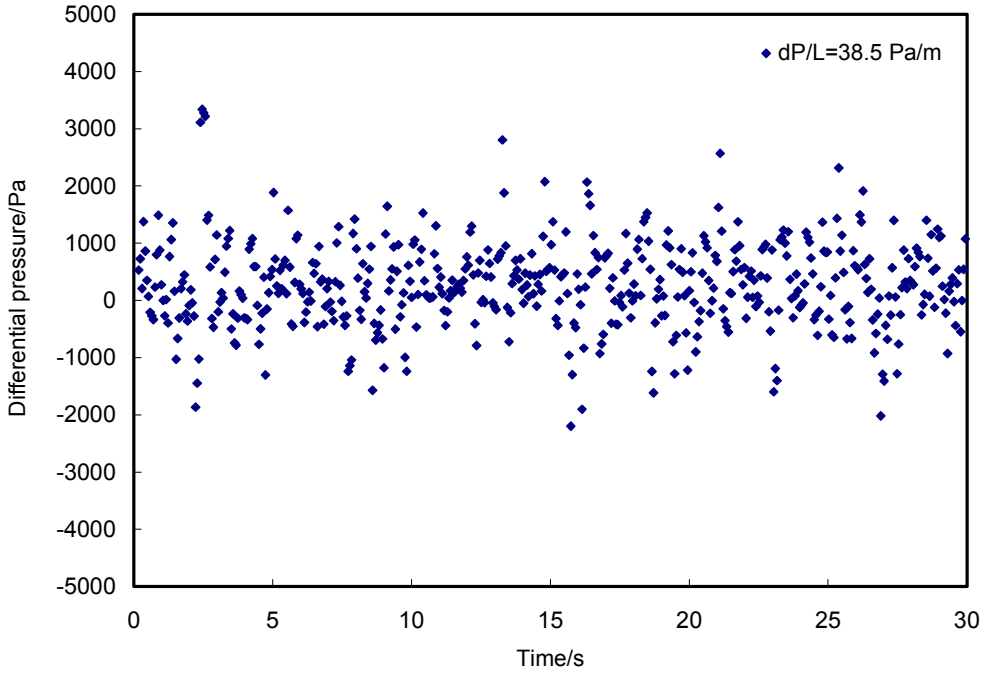

Figure 2. The Differential Pressure Drop at Vsg=10 m/s, Vsl=0.1 m/s, T=90°C, and P=4.45 bar

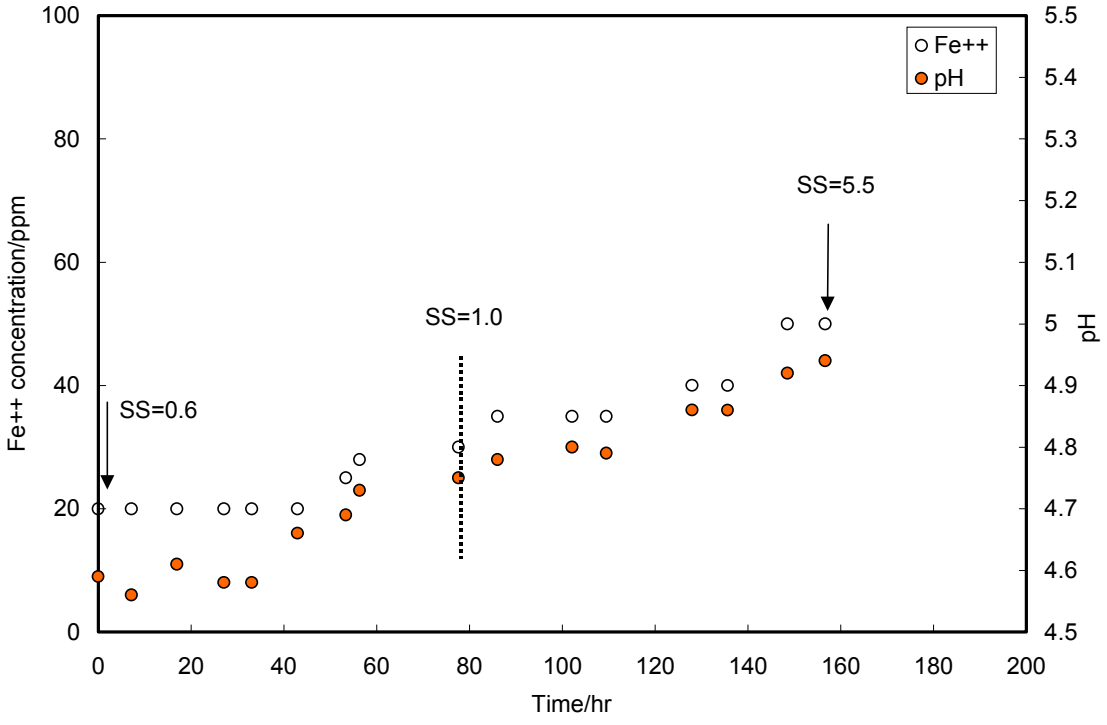

Figure 3. The Change of pH and Fe^{2+} with Time for 0.0% Cl^- solution at Vsg=10 m/s, Vsl=0.1 m/s, T=90°C, and P=4.45 bar (P_{co2}=3.75 bar)

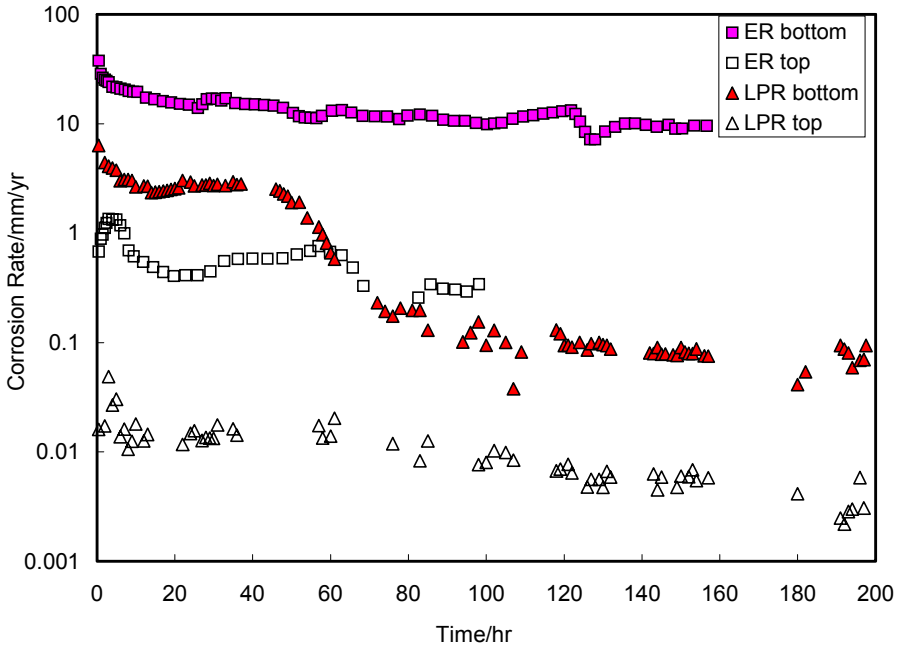

Figure 4. The Change in Corrosion Rate with Time for 0.0% Cl^- Solution at Vsg=10 m/s, Vsl=0.1 m/s, T=90°C, and P=4.45 bar (P_{co2}=3.75 bar)

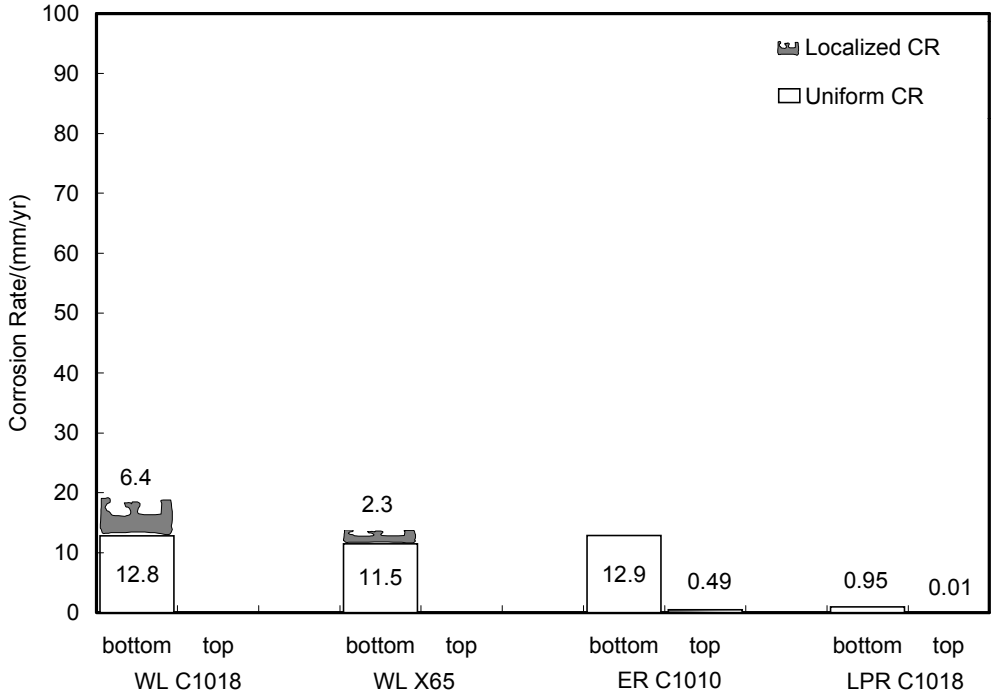

Figure 5. Average Corrosion Rate and Localized Corrosion Rate (LC) from Different Methods for the Experiment without Cl^- at Vsg=10 m/s, Vsl=0.1 m/s, T=90°C, and P=4.45 bar (P_{co2}=3.75 bar)

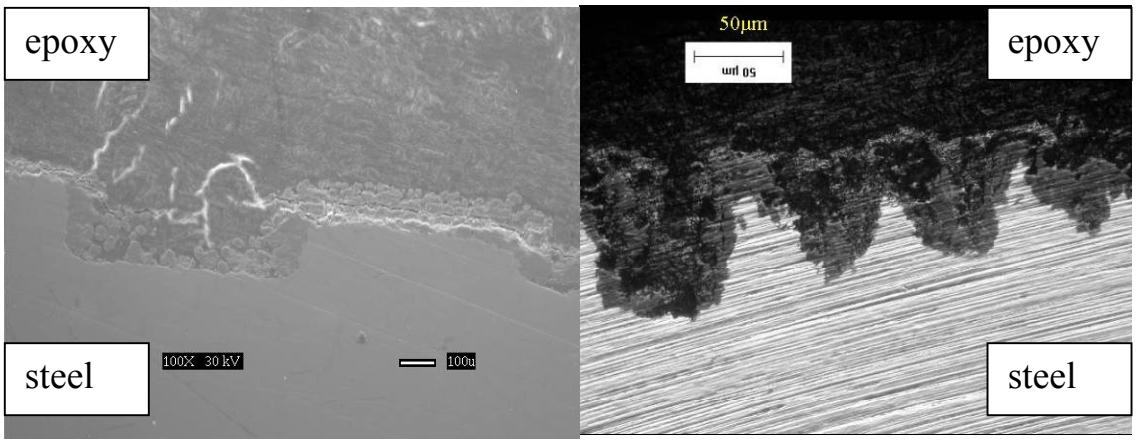

Figure 6. Cross Sections for 0.0% Cl^- Solutions at Vsg=10 m/s, Vsl=0.1 m/s, T=90°C, and P=4.45 bar (P_{co2}=3.75 bar). left: bottom C1018; right: bottom X-65

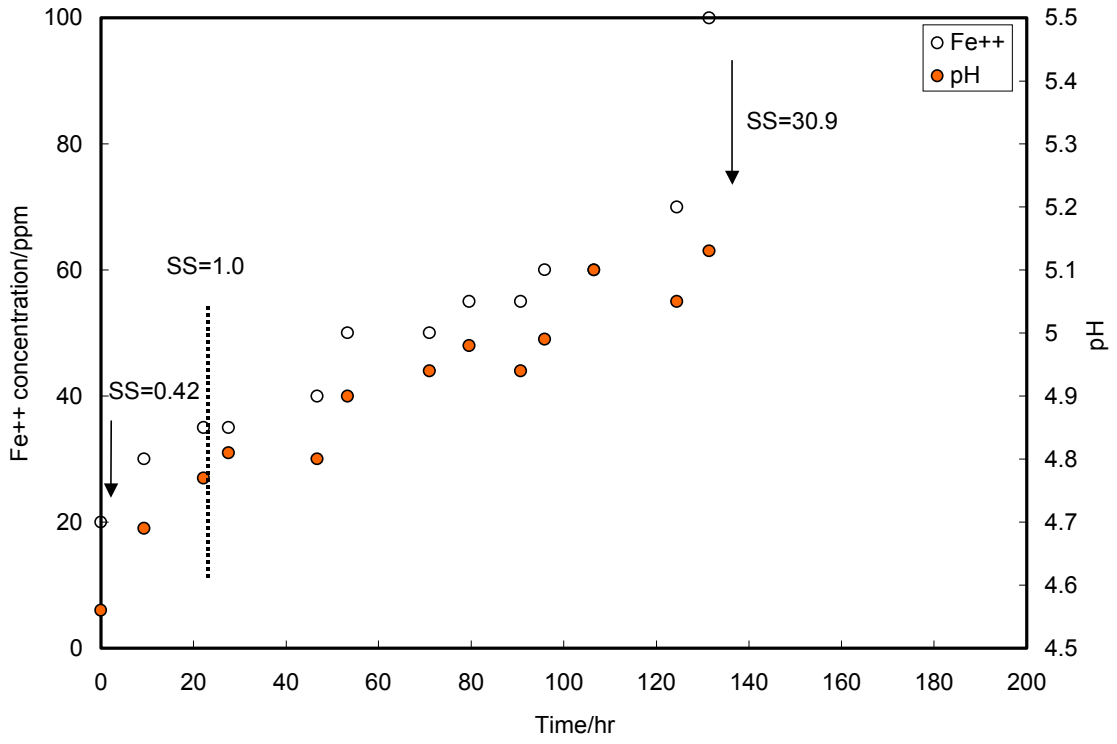

Figure 7. The Change of pH and Fe^{2+} with Time for 0.1% NaCl Solutions at Vsg=10 m/s, Vsl=0.1 m/s, T=90°C, and P=4.45 bar (P_{co2}=3.75 bar)

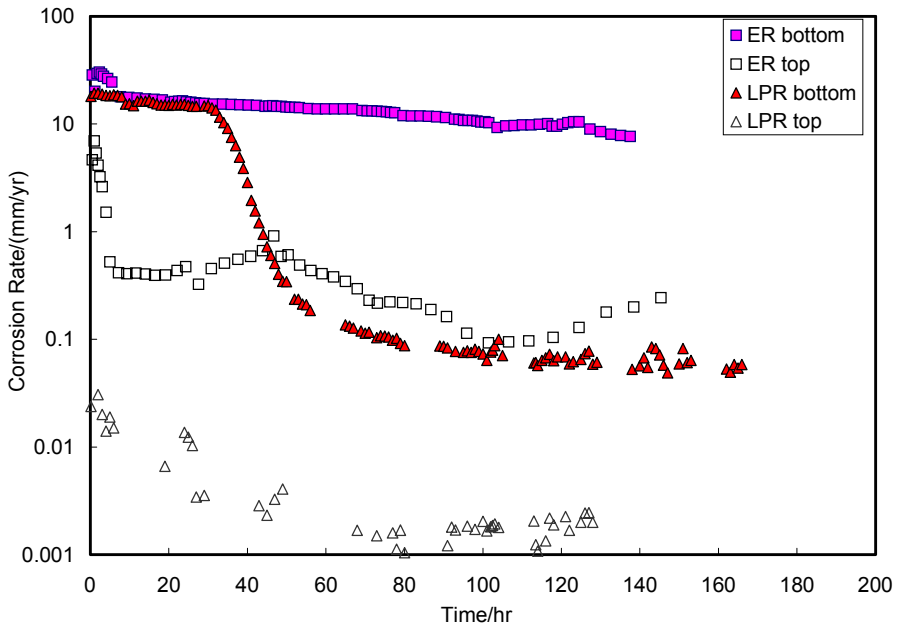

Figure 8. The Change of Corrosion Rate with Time for 0.1% NaCl Solutions at Vsg=10 m/s, Vsl=0.1 m/s, T=90°C, and P=4.45 bar (P_{co2}=3.75 bar)

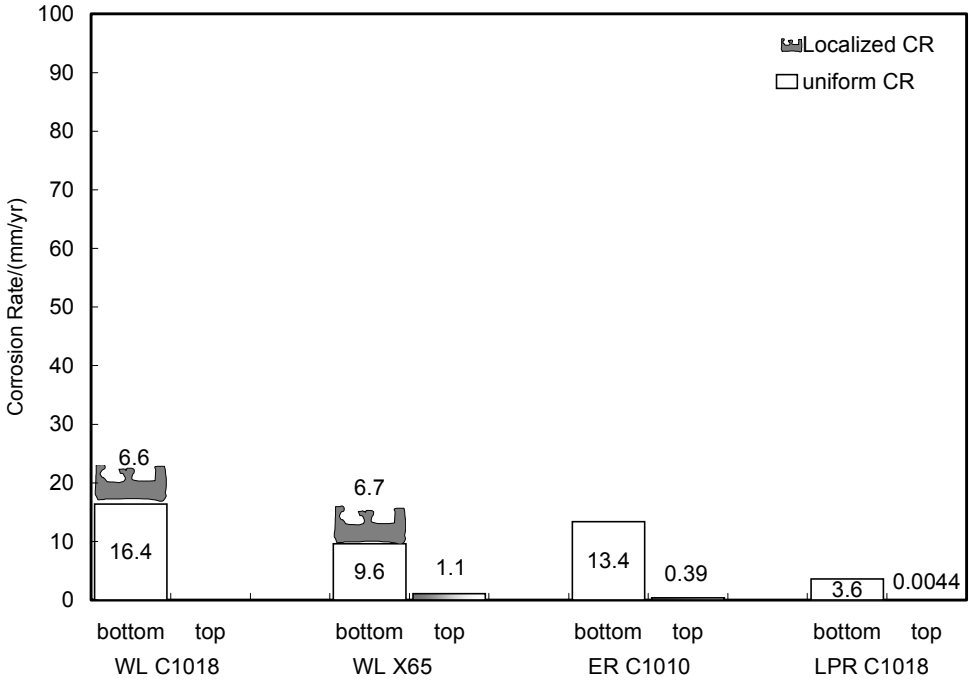

Figure 9. Average and Localized Corrosion Rate (LC) from Different Methods for 0.1% NaCl Solutions at Vsg=10 m/s, Vsl=0.1 m/s, T=90°C, and P=4.45 bar (P_{co2}=3.75 bar)

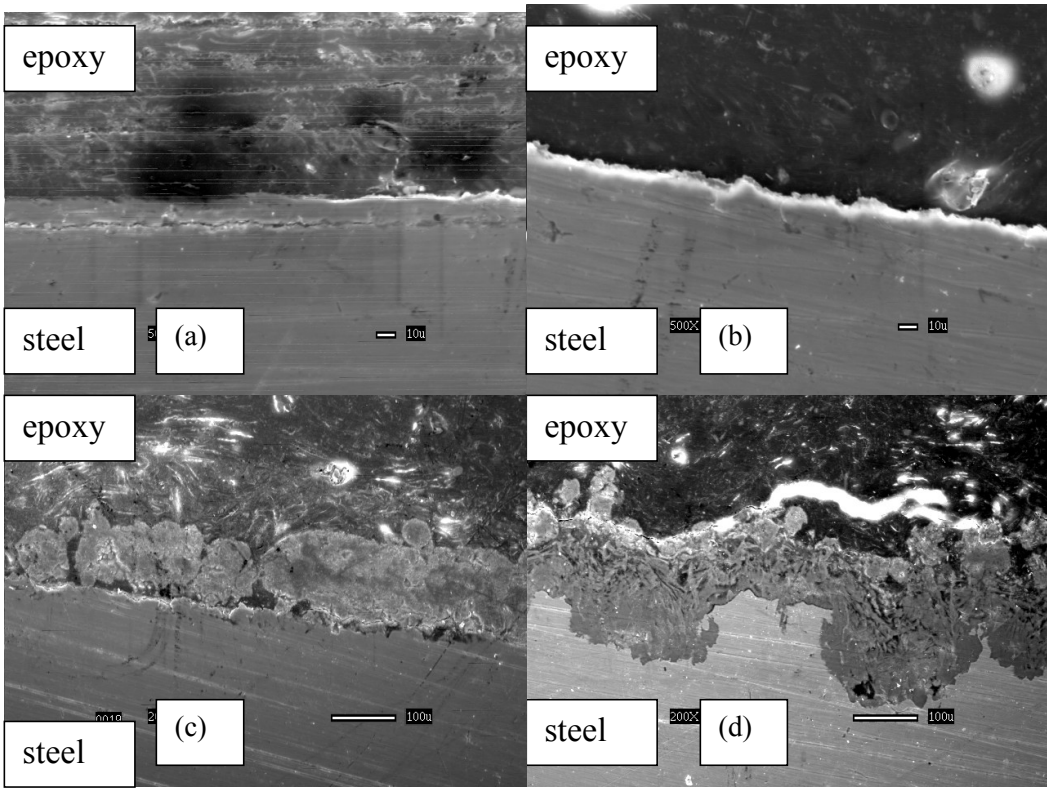

Figure 10. Cross Sections for 0.1% NaCl Solutions at Vsg=10 m/s, Vsl=0.1 m/s, T=90°C, and P=4.45 bar (P_{co2}=3.75 bar). (a) top C1018; (b) top X-65; (c) bottom C1018; (d) bottom X-65

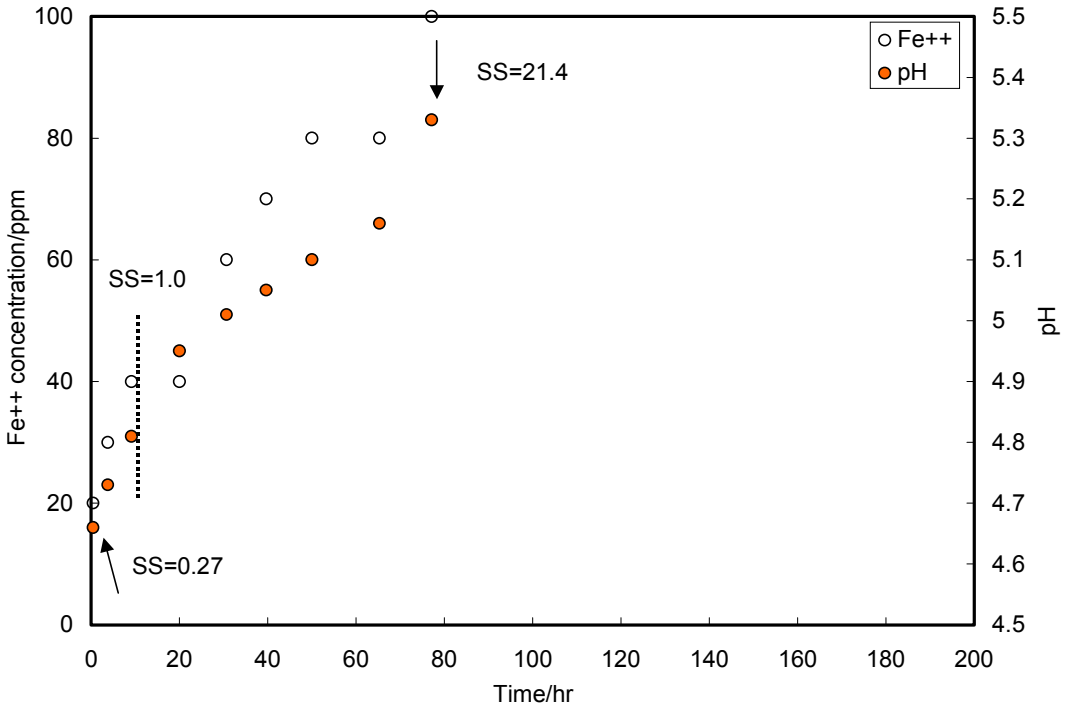

Figure 11. The Change of pH and Fe^{2+} with Time for 1% NaCl Solutions at Vsg=10 m/s, Vsl=0.1 m/s, T=90°C, and P=4.45 bar (P_{co2}=3.75 bar)

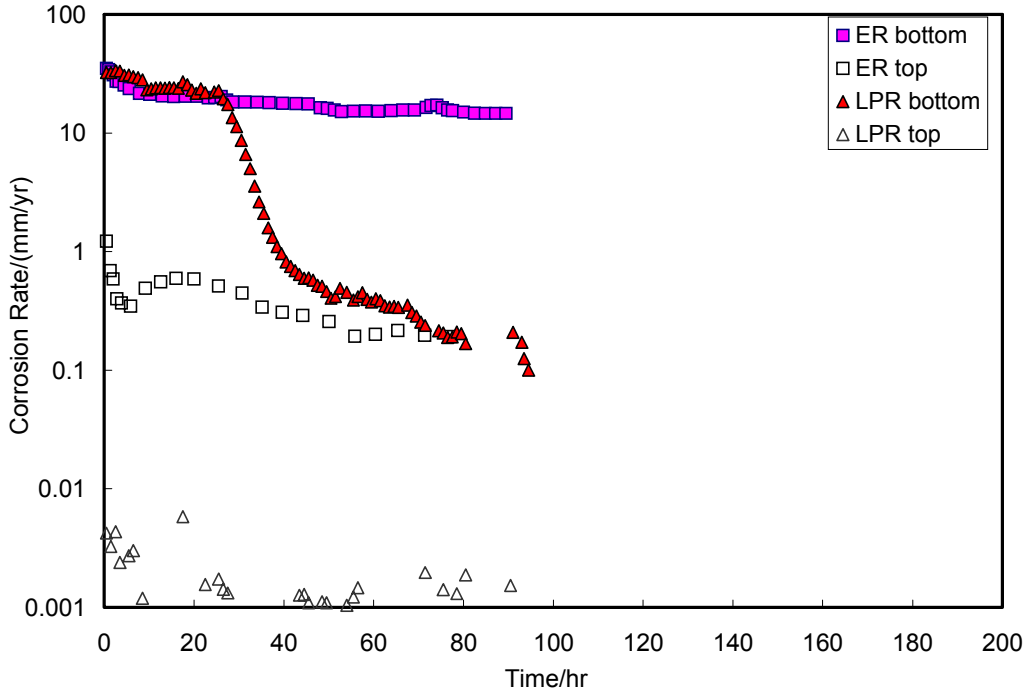

Figure 12. The Change of Corrosion Rate with Time for 1% NaCl Solutions at Vsg=10 m/s, Vsl=0.1 m/s, T=90°C, and P=4.45 bar (P_{co2}=3.75 bar)

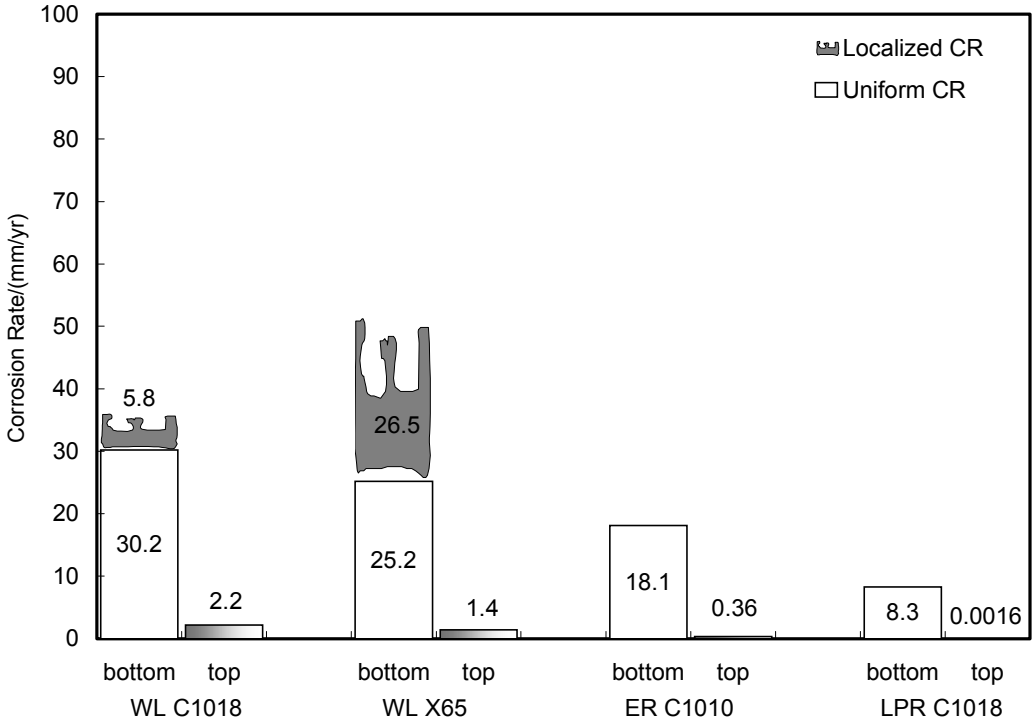

Figure 13. Average and Localized Corrosion Rate (LC) from Different Methods for 1% NaCl Solutions at Vsg=10 m/s, Vsl=0.1 m/s, T=90°C, and P=4.45 bar (P_{co2}=3.75 bar)

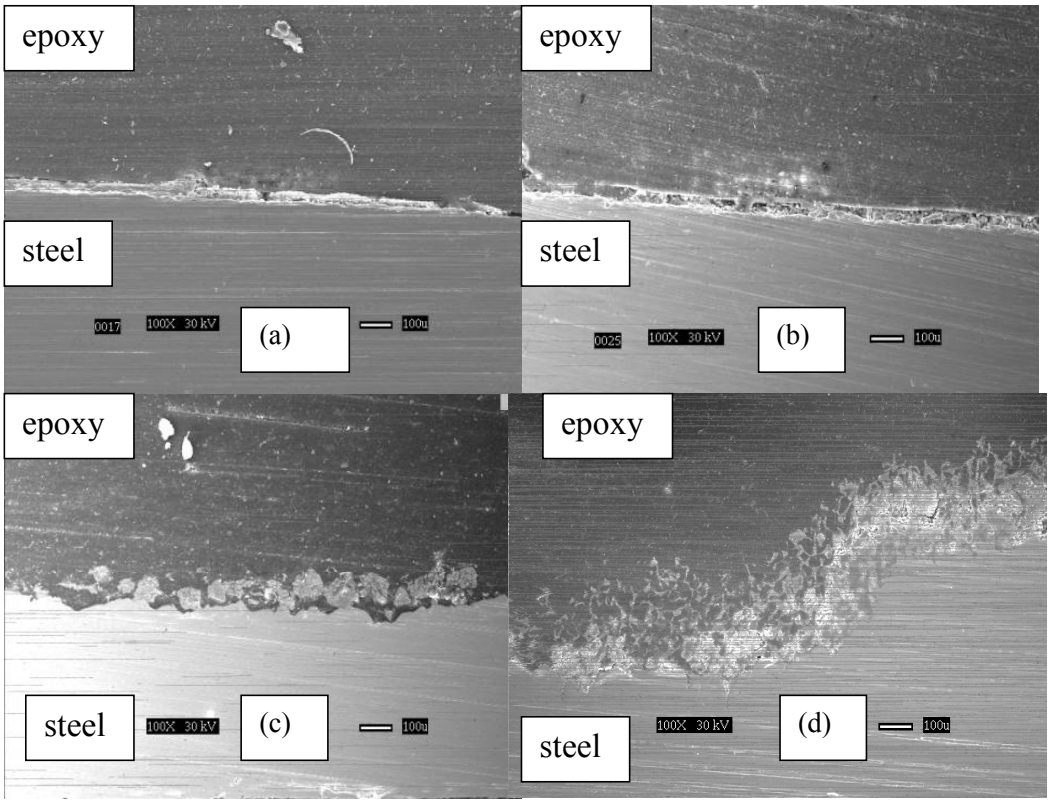

Figure 14. Cross Sections for 1% NaCl Solutions at Vsg=10 m/s, Vsl=0.1 m/s, T=90°C, and P=4.45 bar (P_{co2}=3.75 bar). (a) top C1018; (b) top X-65; (c) bottom ER C1010; (d) bottom X-65

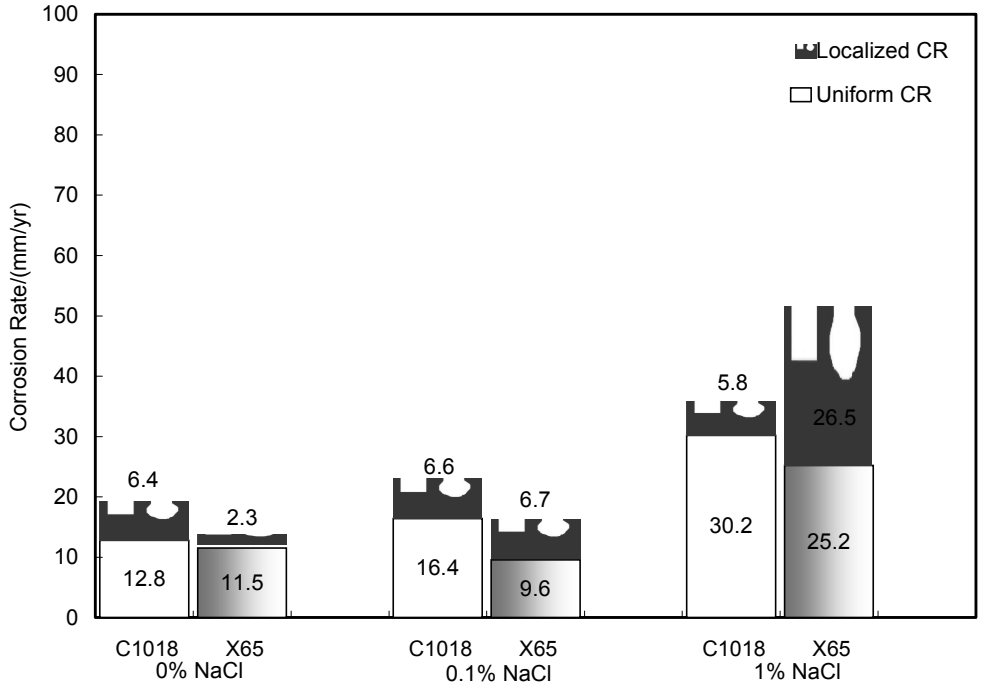

Figure 15. The Effect of NaCl Concentration on Bottom Corrosion for Different Materials from WL Method at Vsg=10 m/s, Vsl=0.1 m/s, T=90°C, and P=4.45 bar (P_{co2}=3.75 bar)

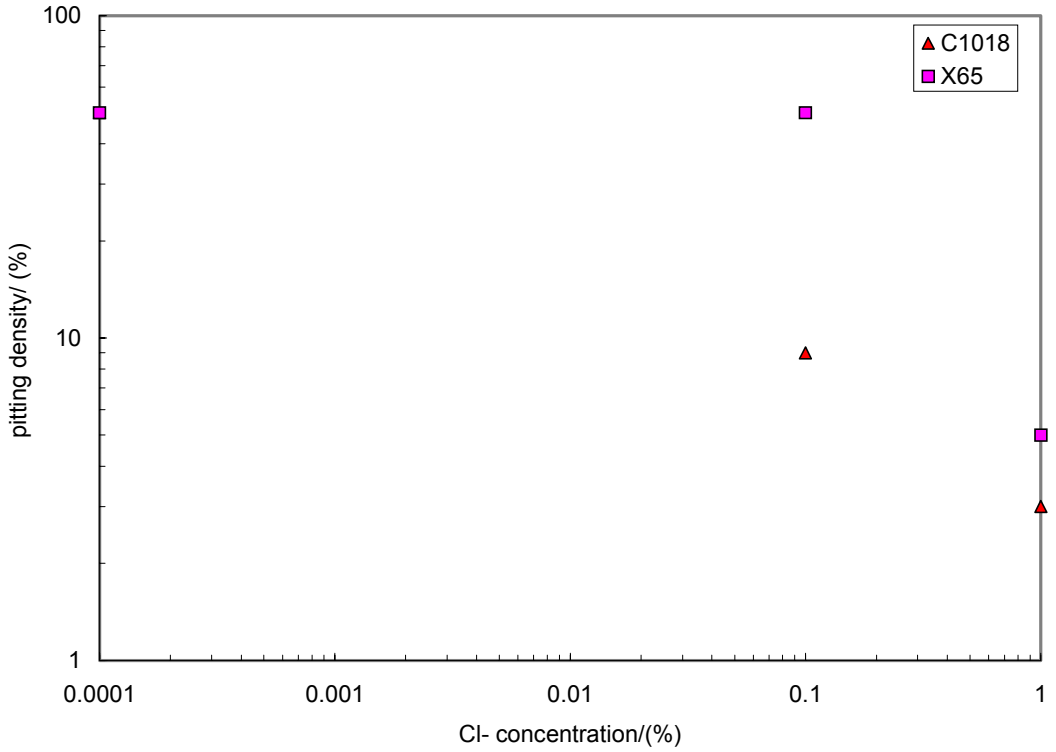

Figure 16. The Effect of Cl- Concentration on Localized Corrosion at Vsg=10 m/s, Vsl=0.1 m/s, T=90°C, and P=4.45 bar (P_{co2}=3.75 bar) (note: 0.0001% Cl^- concentration is used to approximate no Cl^- condition to facilitate the graphical illustration).

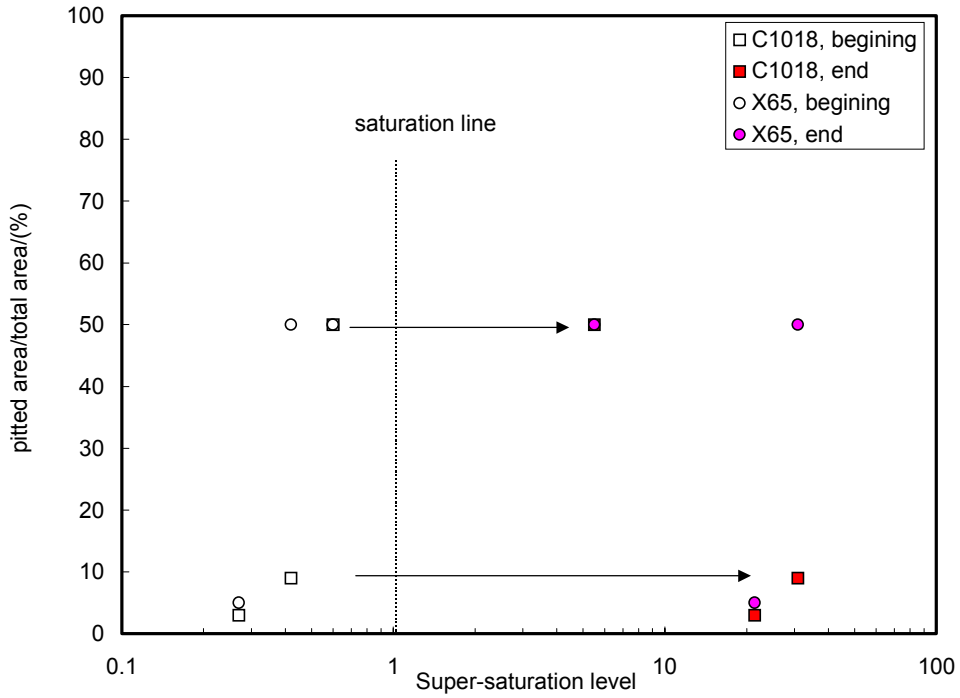

Figure 17. The Relationship Between the Super-Saturation Level and Pitting Density at Vsg=10 m/s, Vsl=0.1 m/s, T=90°C, and P=4.45 bar (P_{co2}=3.75 bar)

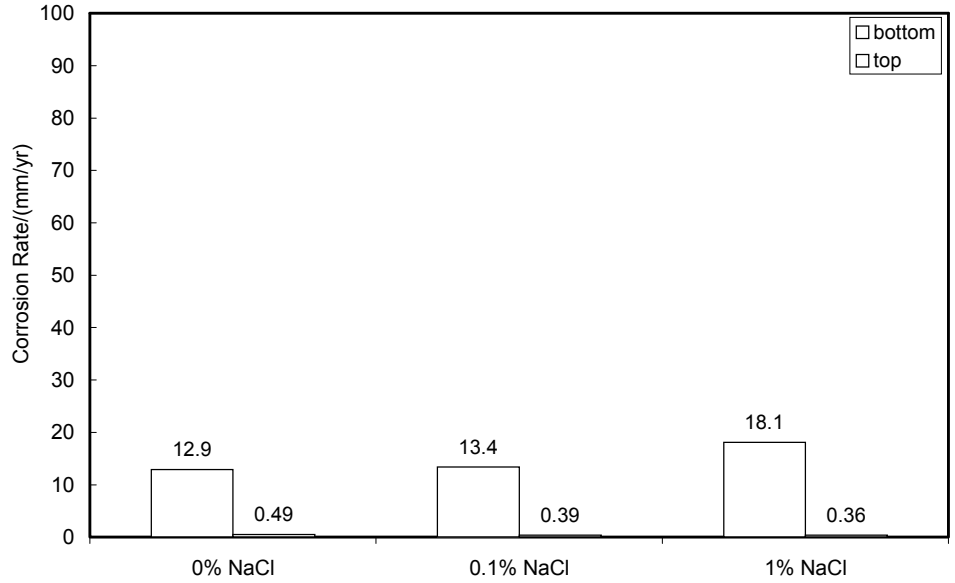

Figure 18. The Effect of NaCl Concentration on the Average Corrosion Rate by ER Measurements at Vsg=10 m/s, Vsl=0.1 m/s, T=90°C, and P=4.45 bar (P_{co2}=3.75 bar)

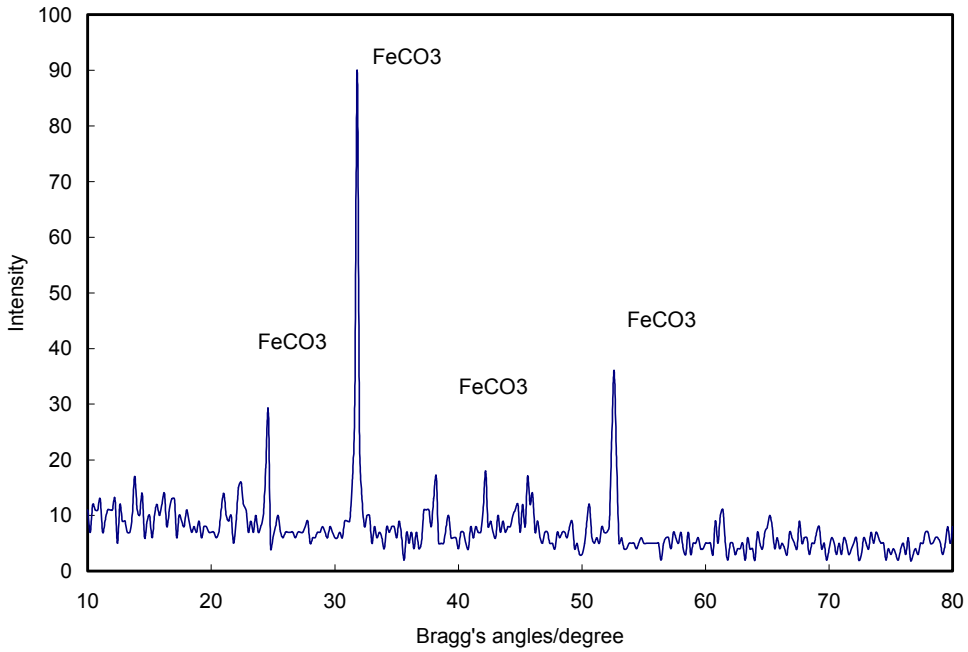

Figure 19. XRD Spectrum for Coupons at Vsg=10 m/s, Vsl=0.1 m/s, T=90°C, and P=4.45 bar (P_{co2}=3.75 bar)

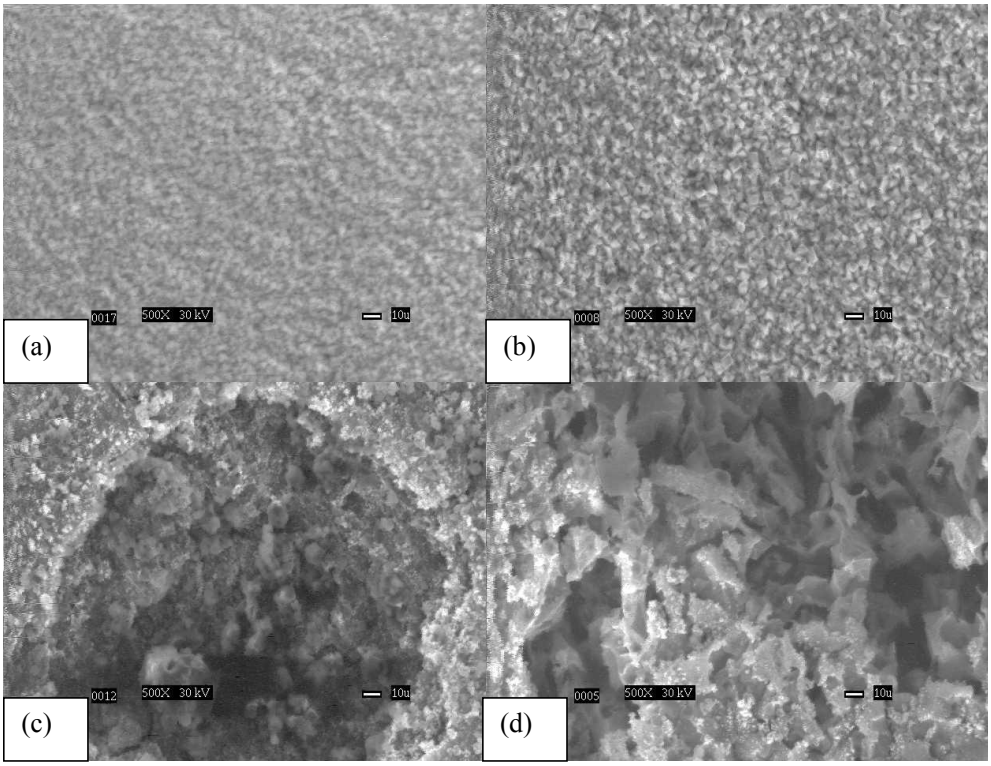

Figure 20. SEM Micrographs for 0.1% NaCl Solutions at Vsg=10 m/s, Vsl=0.1 m/s, T=90°C, and P=4.45 bar (P_{co2}=3.75 bar). (a) top C1018; (b) top X-65; (c) bottom C1018; (d) bottom X65

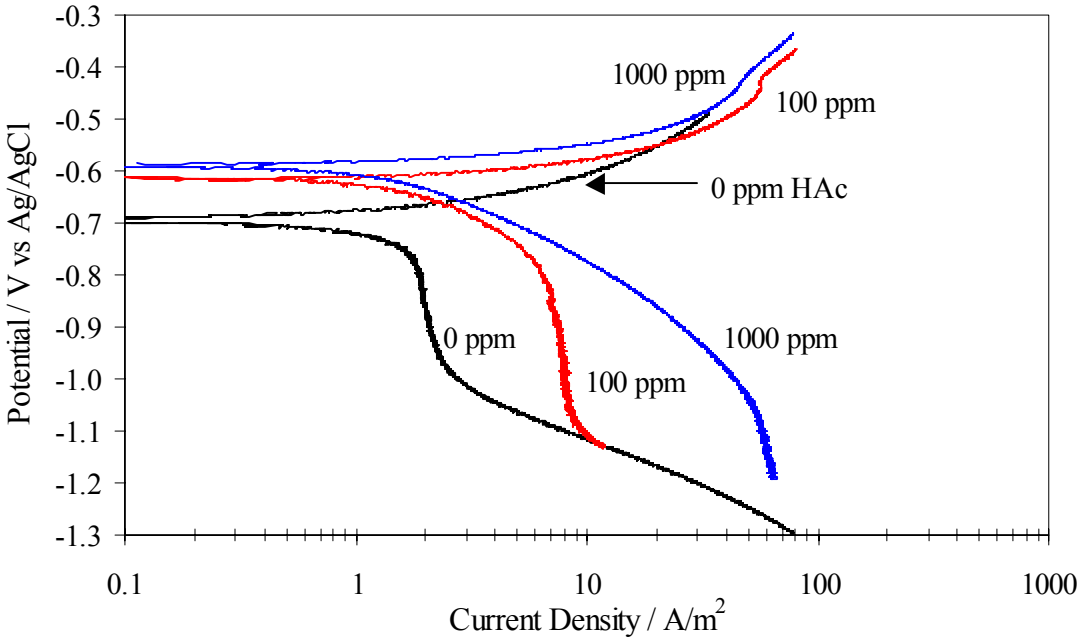

Figure 21. Potentiodynamic Sweeps for 0, 100, and 1000 ppm HAc in Bubbling N_2 Solutions (pH 4, 1000 rpm, 22°C)

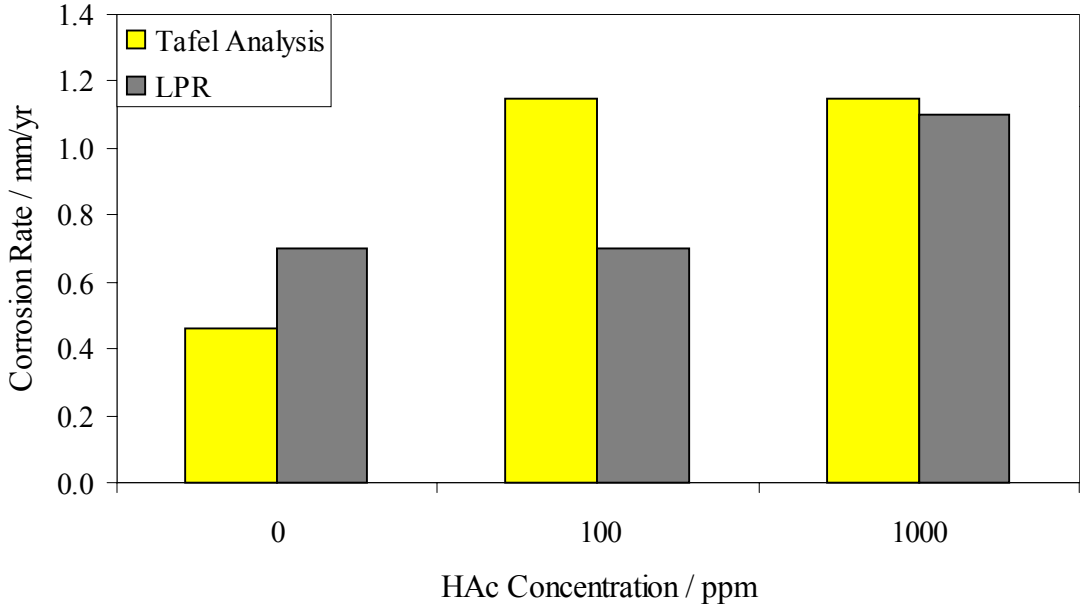

Figure 22. Effect of HAc Concentration on the Corrosion Rate of X-65 Steel in Bubbling N_2 Solutions (pH 4, 1000 rpm, 22°C)

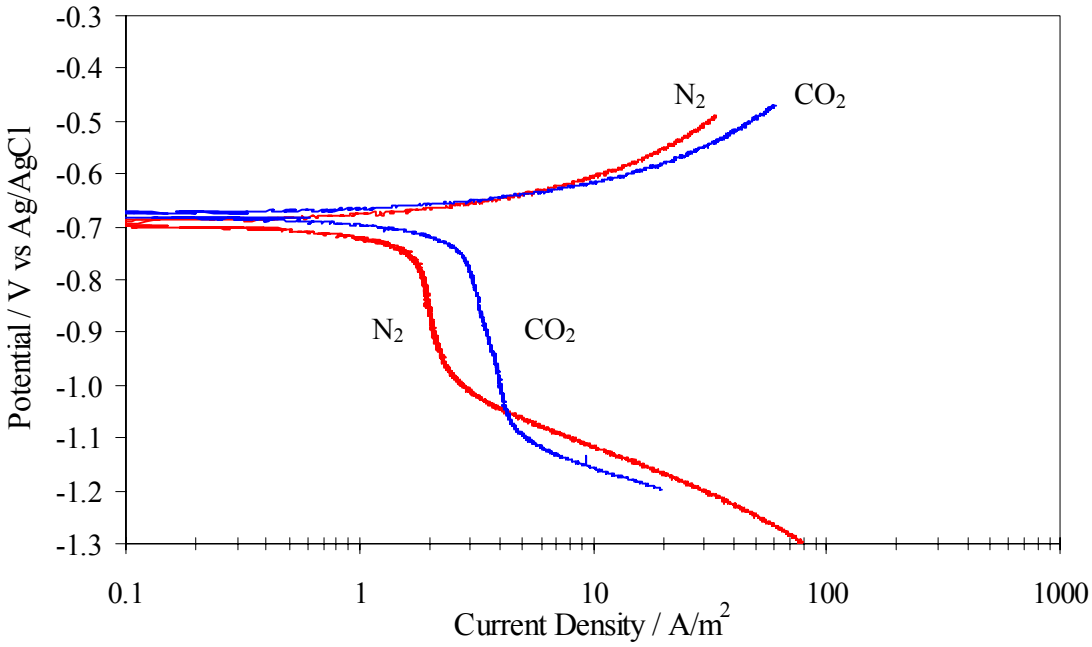

Figure 23. Comparison Between Potentiodynamic Sweeps for 0 ppm HAc in Bubbling CO_2 and N_2 Solutions (pH 4, 1000 rpm, 22°C)

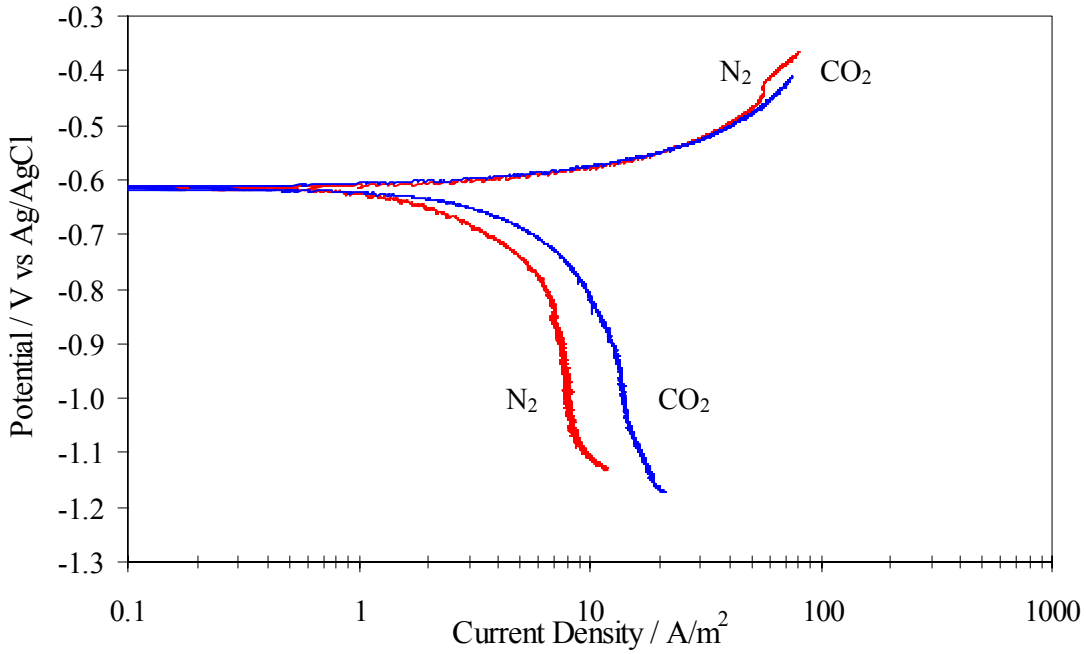

Figure 24. Comparison Between Potentiodynamic Sweeps for 100 ppm HAc in Bubbling CO_2 and N_2 Solutions (pH 4, 1000 rpm, 22°C)

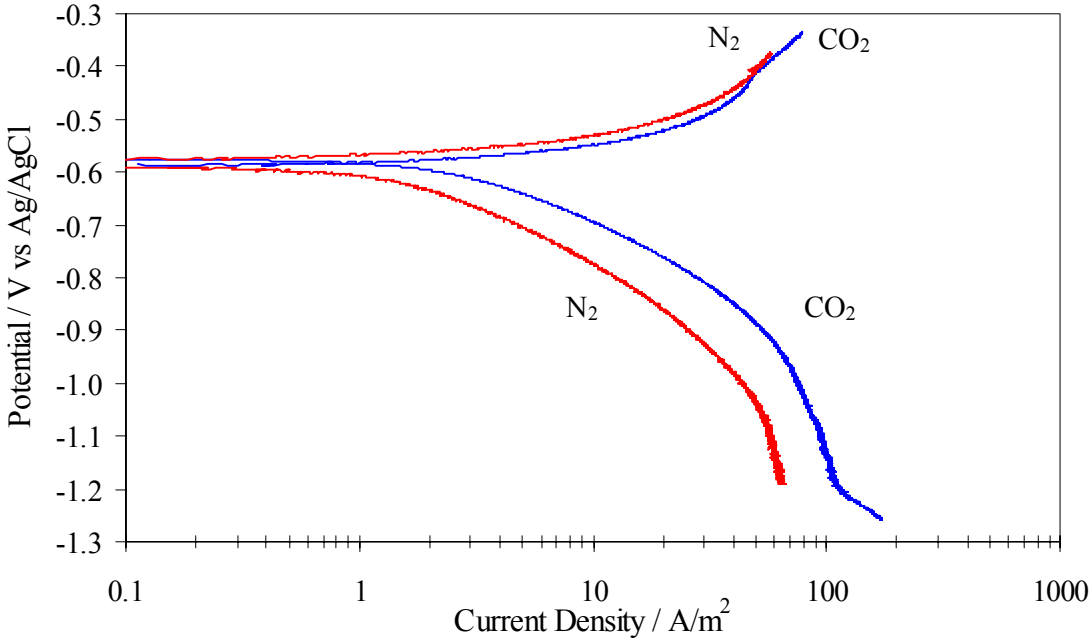

Figure 25. Comparison Between Potentiodynamic Sweeps for 1000 ppm HAc in Bubbling CO_2 and N_2 Solutions (pH 4, 1000 rpm, 22°C)

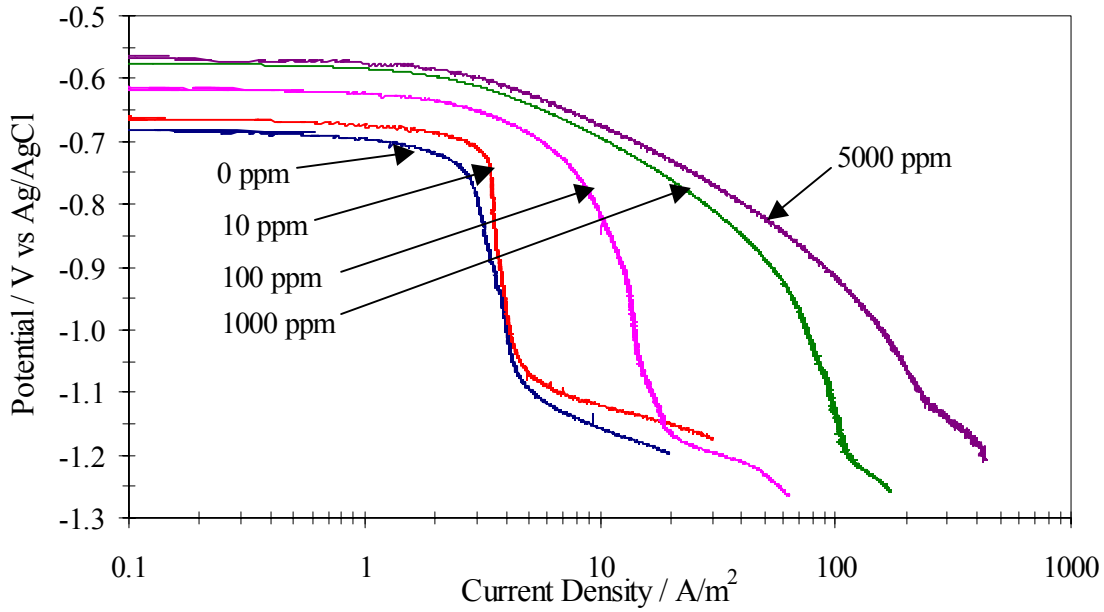

Figure 26. Cathodic Sweeps for 0 – 5000 ppm HAc in Bubbling CO_2 Solutions (pH 4, 1000 rpm, 22°C)

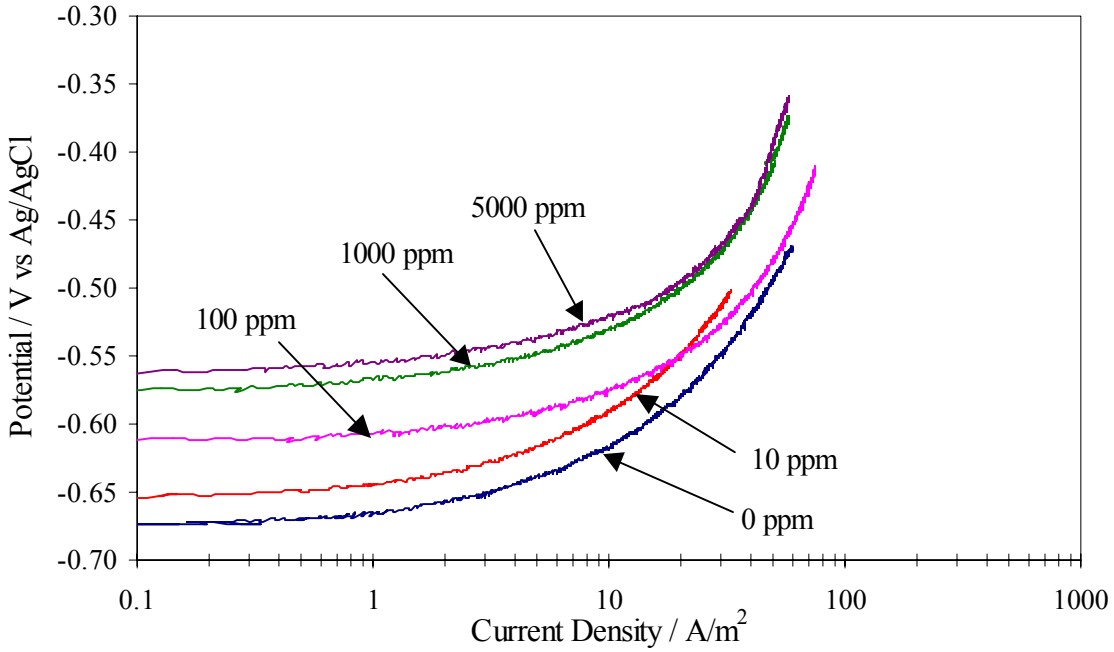

Figure 27. Anodic Sweeps for 0 – 5000 ppm HAc in Bubbling CO_2 Solutions (pH 4, 1000 rpm, 22°C)

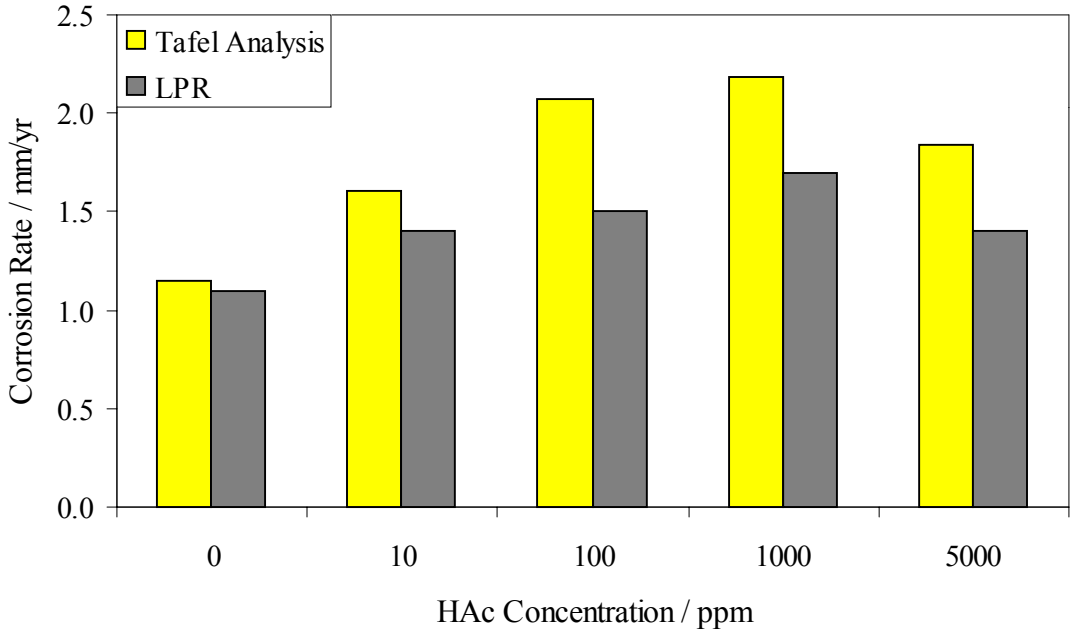

Figure 28. Effect of HAc Concentration on the Corrosion Rate of X-65 Carbon Steel in Bubbling CO_2 Solutions (pH 4, 1000 rpm 22°C)

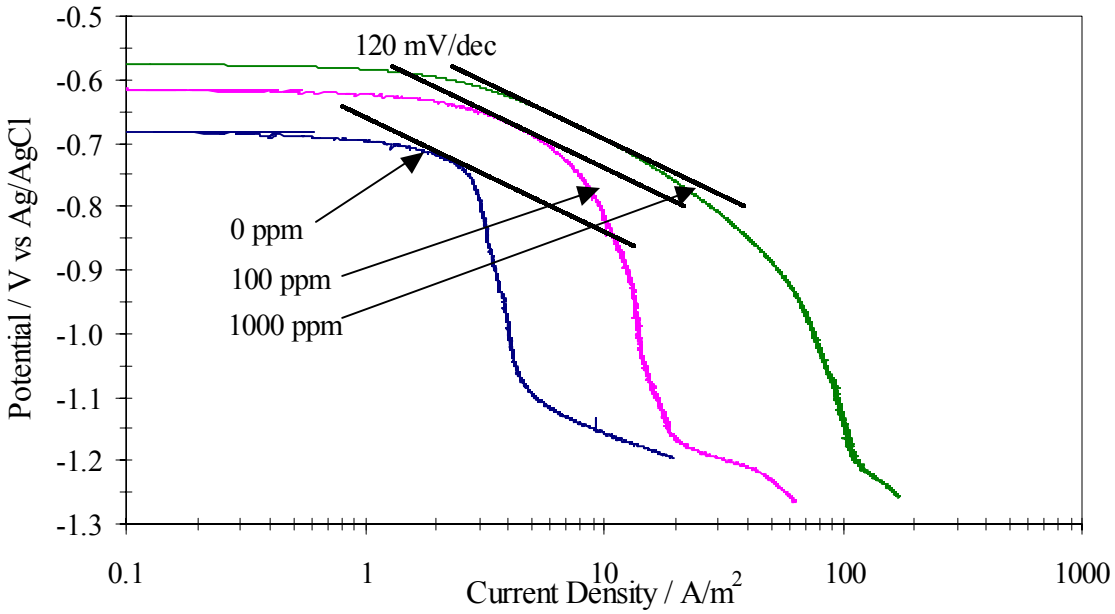

Figure 29. Cathodic Sweeps for Selected HAc Concentrations in Bubbling CO_2 Solutions With Tafel Slopes (22°C, pH 4, 1000 rpm)

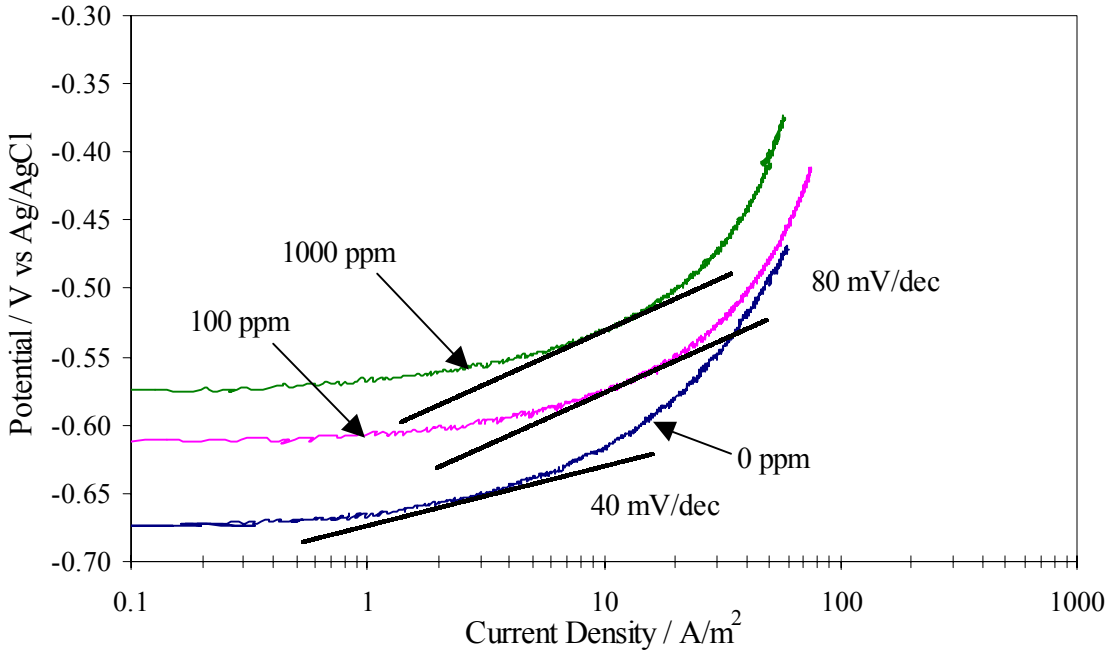

Figure 30. Anodic Sweeps for Selected HAc Concentrations in Bubbling CO_2 Solutions With Tafel Slopes (22°C, pH 4, 1000 rpm)

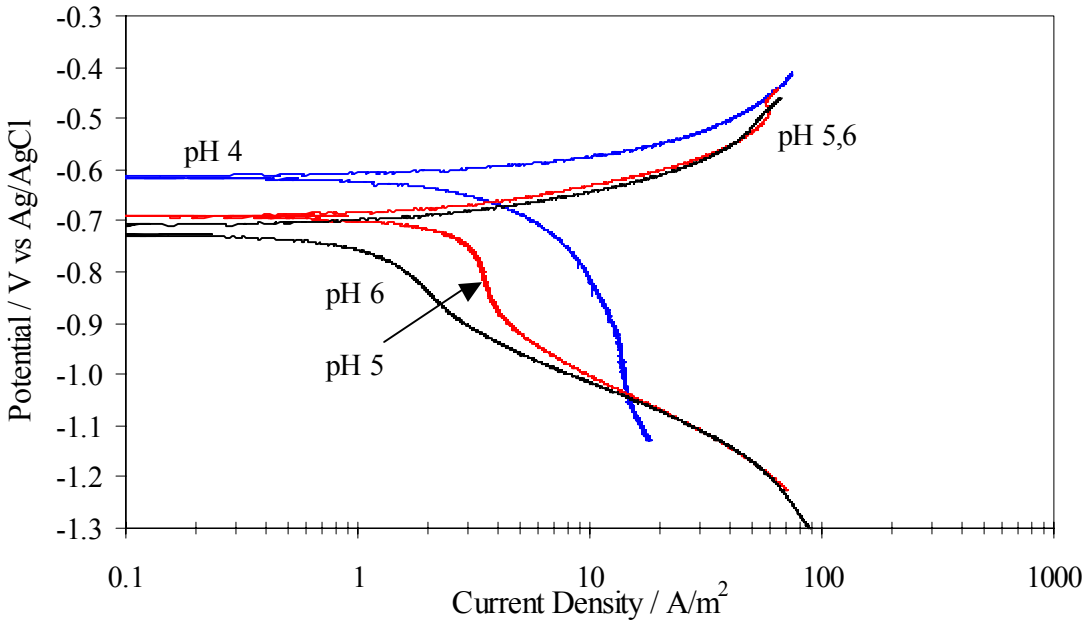

Figure 31. Potentiodynamic Sweeps for 100 ppm HAc in Bubbling CO_2 Solutions at pH 4-6 (1000 rpm, 21°C)

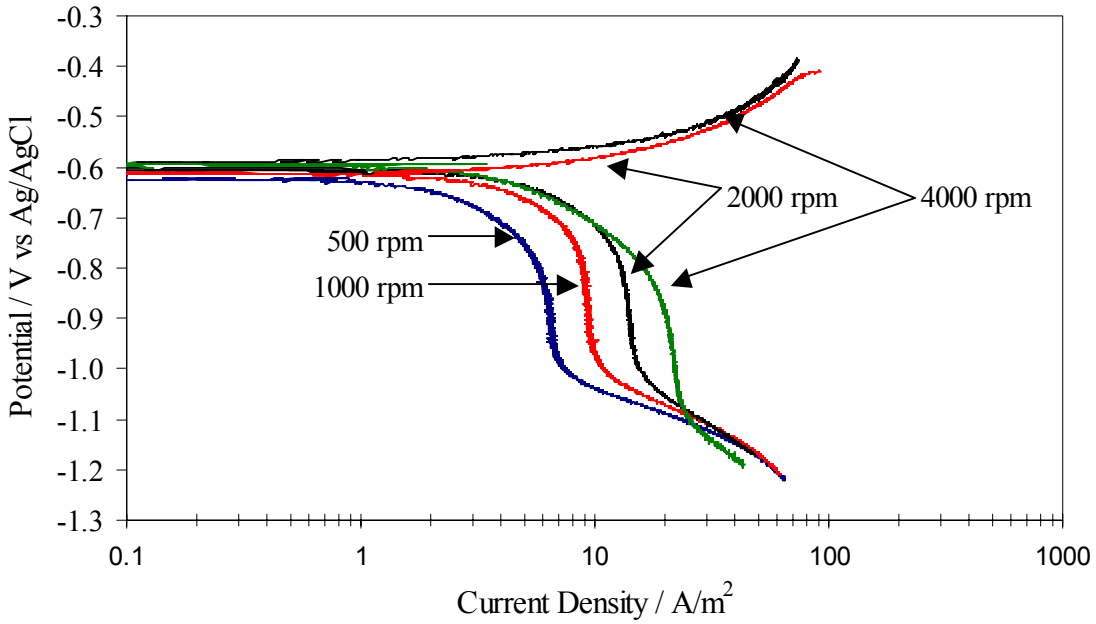

Figure 32. Potentiodynamic Sweeps of 100 ppm HAc in Bubbling CO_2 Solutions at Varying Velocities (pH 4, 21°C)

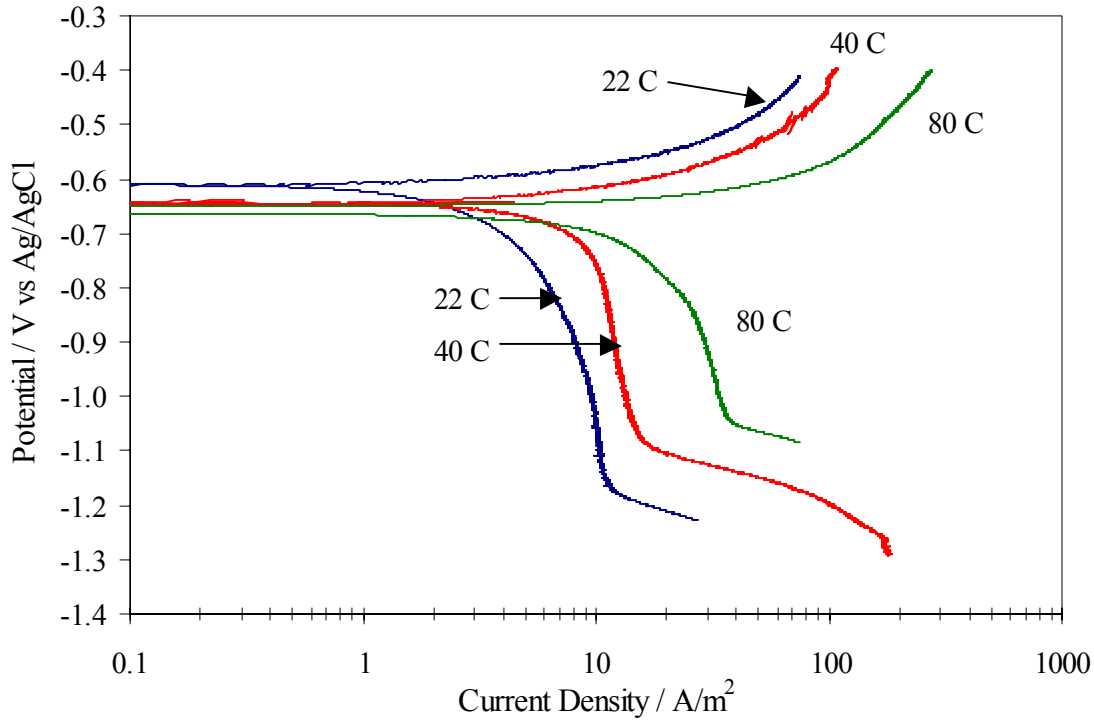

Figure 33. Potentiodynamic Sweeps in Bubbling CO_2 Solutions Containing 100 ppm HAc At Varying Temperatures (pH 4, 1000 rpm)

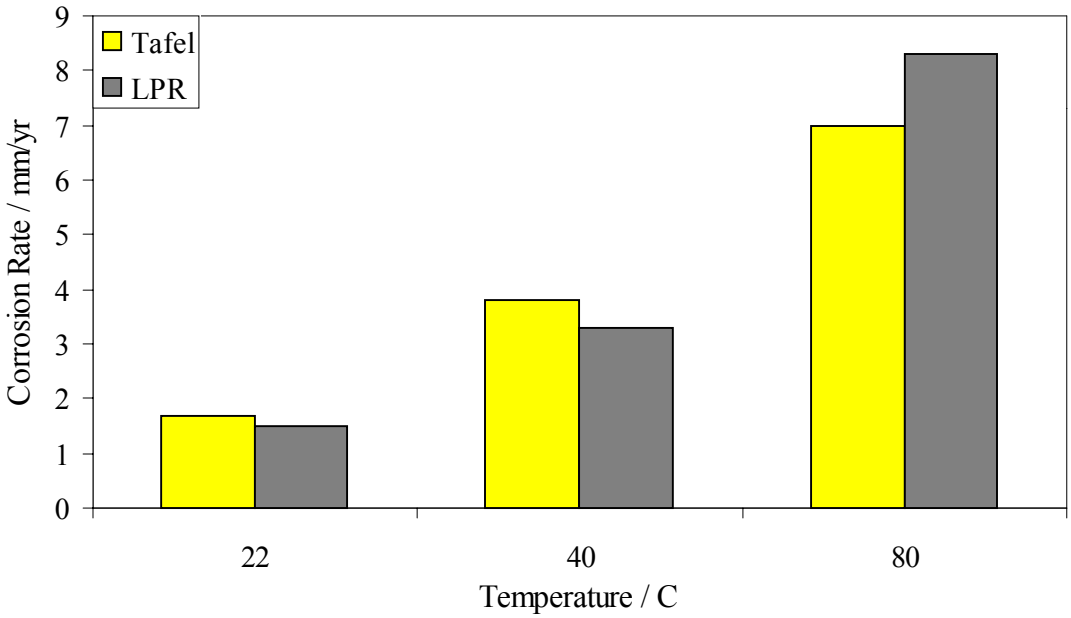

Figure 34. Effect of Temperature on the Corrosion Rate of X-65 Carbon Steel in Bubbling CO_2 Solutions Containing 100 ppm HAc (pH 4, 1000 rpm 22°C)